A&A, 706, A316 (2026)
https://doi.org/10.1051/0004-6361/202558316

Astronomy & Astrophysics

Expanding the $C_3H_6O_2$ isomeric interstellar inventory: Discovery of lactaldehyde and methoxyacetaldehyde in G+0.693-0.027

M. Sanz-Novo[1,⋆], V. M. Rivilla[1], I. Jiménez-Serra[1], L. Colzi[1], S. Zeng[2], A. Megías[1], D. San Andrés[1,3], Á. López-Gallifa[1], A. Martínez-Henares[1], Z. T. P. Fried[4], B. A. McGuire[4,5], S. Martín[6,7], M. A. Requena-Torres[8], B. Tercero[9,10], P. de Vicente[10], L. Kolesniková[11], E. R. Alonso[12], E. J. Cocinero[13,14], J. C. Guillemin[15], and I. Kleiner[16]

[1] Centro de Astrobiología (CAB), INTA-CSIC, Carretera de Ajalvir km 4, Torrejón de Ardoz, 28850 Madrid, Spain
[2] Star and Planet Formation Laboratory, Pioneering Research Institute, RIKEN, 2-1 Hirosawa, Wako, Saitama 351-0198, Japan
[3] Departamento de Física de la Tierra y Astrofísica, Facultad de Ciencias Físicas, Universidad Complutense de Madrid, 28040 Madrid, Spain
[4] Massachusetts Institute of Technology, Cambridge, MA 02139, USA
[5] National Radio Astronomy Observatory, Charlottesville, VA 22903, USA
[6] European Southern Observatory, Alonso de Córdova 3107, Vitacura 763 0355, Santiago, Chile
[7] Joint ALMA Observatory, Alonso de Córdova 3107, Vitacura 763 0355, Santiago, Chile
[8] Department of Physics, Astronomy and Geosciences, Towson University, Towson, MD 21252, USA
[9] Observatorio Astronómico Nacional (OAN-IGN), Calle Alfonso XII 3, 28014 Madrid, Spain
[10] Observatorio de Yebes (OY-IGN), Cerro de la Palera SN, Yebes, Guadalajara, Spain
[11] Department of Analytical Chemistry, University of Chemistry and Technology, Technická 5, 166 28 Prague 6, Czechia
[12] Grupo de Espectroscopía Molecular, Edificio Quifima, Parque Científico UVa, Universidad de Valladolid, Valladolid, 47005 Spain
[13] Departamento de Química Física, Facultad de Ciencia y Tecnología, Universidad del País Vasco (EHU), 48940 Leioa, Spain
[14] Instituto Biofisika (CSIC, EHU), 48940 Leioa, Spain
[15] Univ Rennes, Ecole Nationale Supérieure de Chimie de Rennes, CNRS, ISCR-UMR6226, 35000 Rennes, France
[16] Université Paris Cité and Univ Paris Est Creteil, CNRS, LISA, 75013 Paris, France

Received 28 November 2025 / Accepted 9 January 2026

ABSTRACT

Aims. The tentative detection of 3-hydroxypropanal ($HO(CH_2)_2C(O)H$) toward the Galactic center molecular cloud G+0.693-0.027 prompts a systematic survey in this source aimed at detecting all $C_3H_6O_2$ isomers with available spectroscopy.
Methods. We used an ultra-deep broadband spectral survey of G+0.693-0.027, carried out with the Yebes 40 m and IRAM 30 m telescopes, to conduct the astronomical search.
Results. We report the first interstellar detection of lactaldehyde ($CH_3CH(OH)C(O)H$) and methoxyacetaldehyde ($CH_3OCH_2C(O)H$), together with the second detections (i.e., confirmation) of methyl acetate ($CH_3C(O)OCH_3$) and hydroxyacetone ($CH_3C(O)CH_2OH$), and new detections in this source of both *anti*- and *gauche*- conformers of ethyl formate ($CH_3CH_2OC(O)H$; the latter being tentative). For these species, we derived a fractional abundance relative to H_2 of ∼(0.81, 0.24, 16, 1.6, 1.3, 1.4) × 10^{-10}, respectively. In contrast, neither propionic acid, $CH_3CH_2C(O)OH$, nor glycidol, c-CH_2OCHCH_2OH (i.e., the most and the least stable species within the $C_3H_6O_2$ family, respectively) were detected, and we provide upper limits on their fractional abundances of ≤1.5 × 10^{-10} and ≤3.7 × 10^{-11}. Interestingly, all $C_3H_6O_2$ isomers can be synthesized through radical–radical reactions on the surface of dust grains, ultimately tracing back to CO as the parent molecule. We suggest that formation of the detected isomers is mainly driven by successive hydrogenation of CO, producing CH_3OH and CH_3CH_2OH as the primary parent species. Conversely, propionic acid is thought to originate from the oxygenation of CO via the HOCO intermediate, which help us rationalize its non-detection. Overall, our findings notably expand the known chemical inventory of the interstellar medium and provide direct observational evidence that increasingly complex chemistry involving O-bearing species occurs in space.

Key words. astrochemistry – line: identification – molecular data – ISM: molecules – ISM: individual objects: G+0.693-0.027

1. Introduction

Structural isomerism, in which molecules share an identical molecular formula but differ in the connectivity of their constituent atoms, represents a fundamental source of chemical diversity in the interstellar medium (ISM). From a chemical point of view, this diversity translates into distinct isomers often exhibiting markedly different electronic structures, thermodynamic stabilities, and spectroscopic signatures, making the identification of individual isomers a valuable tool for distinguishing among their plausible formation pathways (Shingledecker et al. 2019; Neill et al. 2012; Marcelino et al. 2021; Rivilla et al. 2023; García de la Concepción et al. 2023; San Andrés et al. 2024; Remijan et al. 2025; Sanz-Novo et al. 2025).

Within this context, the $C_3H_6O_2$ isomeric family has garnered particular attention in recent years from the

⋆ Corresponding author: miguel.sanz.novo@cab.inta-csic.es

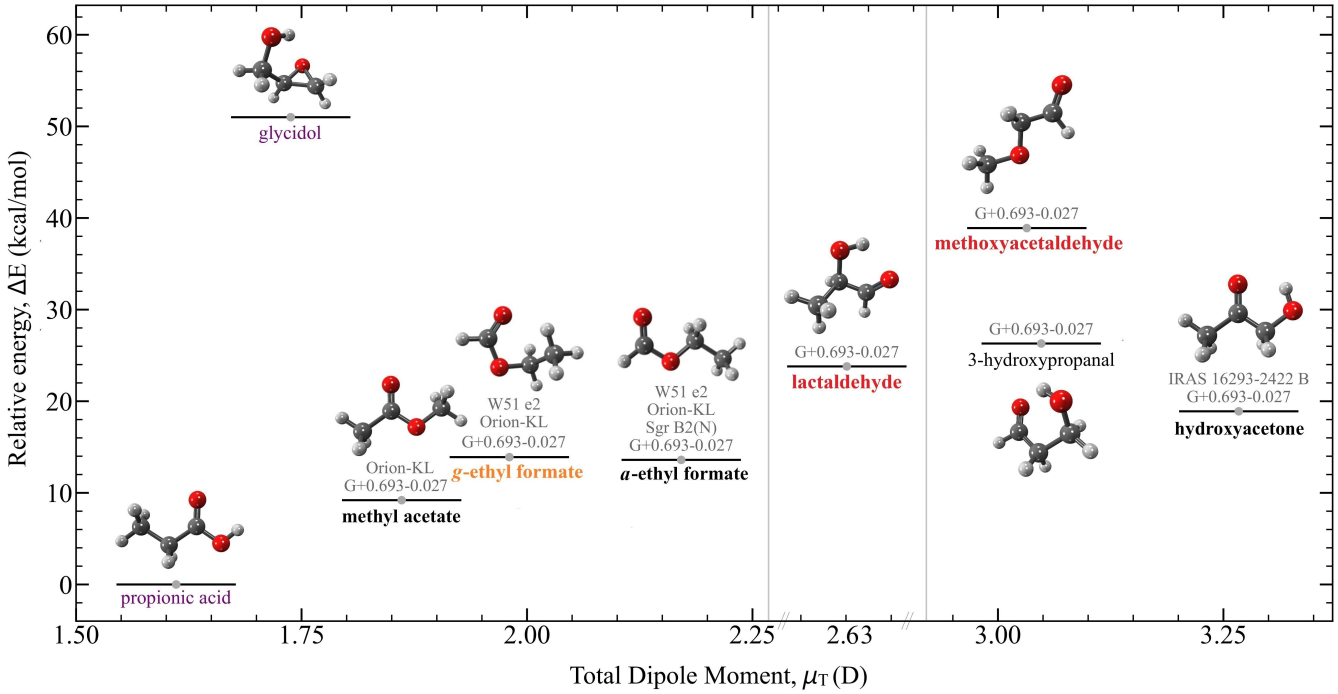

Fig. 1. Relative energies (including zero-point energy, ZPE, corrections) plotted as a function of the total dipole moment for the targeted $C_3H_6O_2$ isomers, computed at the B2PLYPD3/aug-cc-pVTZ level of theory (Grimme et al. 2011) using the Gaussian 16 program package (Frisch et al. 2016). Optimized 3D structures at the same level of theory are also shown (carbon atoms in gray, oxygen atoms in red, and hydrogen atoms in white). The status of detections in G+0.693 is indicated using the following color-code in the molecule name: new first detections in the ISM are shown in red, tentative detections in orange, non-detections in purple, and previous detections toward different sources in black. Previous detections toward other sources of methyl acetate (Tercero et al. 2013), *anti* and *gauche* ethyl formate (Belloche et al. 2009; Tercero et al. 2013; Rivilla et al. 2017; Peng et al. 2019), hydroxyacetone (Zhou et al. 2020), and 3-hydroxypropanal are also included. Also, new detections based in this work are highlighted in boldface. The 3D representations of all molecules are visualized with IQmol (`https://www.iqmol.org/`).

astrochemical community (Savarese et al. 2025). It encompasses molecules with diverse functional groups, ranging from families that are widespread in nature such as aldehydes (i.e., 2-hydroxypropanal or lactaldehyde, $CH_3CH(OH)C(O)H$, 3-hydroxypropanal, $HO(CH_2)_2C(O)H$, and methoxyacetaldehyde, $CH_3OCH_2C(O)H$), esters (i.e., methyl acetate, $CH_3C(O)OCH_3$, and ethyl formate, $CH_3CH_2OC(O)H$), ketones (hydroxyacetone, $CH_3C(O)CH_2OH$), and carboxylic acids (propionic acid, $CH_3CH_2C(O)OH$), to more structurally exotic compounds such as epoxy alcohols (glycidol, c-CH_2OCHCH_2OH), diols, and enediols (i.e., prop-1-ene-1,2-diol, $CH_3C(OH)CHOH$, prop-2-ene-1,2-diol, $CH_2C(OH)CH_2OH$, and prop-1-ene-1,3-diol, $HOCH_2CHCHOH$).

Identifying which of these isomers are present in the ISM requires the synergy of accurate high-resolution laboratory rotational data, sensitive astronomical observations, and astrochemical modeling. These combined efforts have thus far yielded the detection of both the *anti* and *gauche* conformers of ethyl formate (Belloche et al. 2009; Tercero et al. 2013; Rivilla et al. 2017; Peng et al. 2019), methyl acetate (Tercero et al. 2013), and hydroxyacetone (Zhou et al. 2020) toward various star-forming regions, as well as the recent tentative detection of 3-hydroxypropanal toward the Galactic center (GC) molecular cloud G+0.693-0.027 (hereafter G+0.693, Fried et al. 2025). Meanwhile, fruitless searches have been reported for propionic acid, the global minimum in energy, and for higher energy isomers such as methoxyacetaldehyde and lactaldehyde in Orion KL and Sagittarius B2(N) (Ilyushin et al. 2021; Belloche et al. 2025; Alonso et al. 2019; Kolesniková et al. 2018).

In the laboratory, experiments have shown that multiple $C_3H_6O_2$ isomers can form under typical astrophysical conditions. Wang et al. (2023) reported the production of hydroxyacetone, methyl acetate, and 3-hydroxypropanal -all of which have already been identified in the ISM- along with their enol tautomers in UV-irradiated methanol–acetaldehyde ices, offering insights into their possible formation pathways. In a subsequent study, Wang et al. (2024) demonstrated that the irradiation of CO–ethanol ices yields, in addition to the known interstellar species ethyl formate and 3-hydroxypropanal, other isomers still uncharted in the ISM, such as 1,3-propenediol and lactaldehyde.

In light of these findings, a systematic survey of all the spectroscopically characterized $C_3H_6O_2$ isomers (see Figure 1) will be essential for expanding the known interstellar chemical inventory of complex organic molecules (COMs, defined as carbon-based molecules comprised of six or more atoms; Herbst et al. 2020) and for unveiling whether a particularly complex, yet unknown underlying chemistry involving relatively large O-bearing species occurs in space.

Over the last few years, the search for COMs has increasingly turned toward unusual environments in the GC such as the GC molecular cloud G+0.693. This cloud appears as one of the most compelling sources for the potential detection of the remaining $C_3H_6O_2$ isomers, as supported by the growing inventory of COMs discovered in it (see, e.g., Rivilla et al. 2023; Sanz-Novo et al. 2025). It includes new complex O-bearing species with one C atom such as *cis*-carbonic acid (HOCOOH; Sanz-Novo et al. 2023), two C atoms such as (*Z*)-1,2-ethenediol ($(CHOH)_2$, Rivilla et al. 2022a) and *trans*-methyl formate (CH_3OCHO;

Table 1. Derived physical parameters for $C_3H_6O_2$ isomers that we searched for toward G+0.693-0.027.

Molecule	Formula	ΔE^a (kcal mol^{-1}/K)	μ(tot)^a (D)	N ($\times10^{13}$ cm^{-2})	T_{ex} (K)	v_{LSR} (km s^{-1})	FWHM (km s^{-1})	Abundance^b ($\times10^{-10}$)	Status^c
propionic acid	$CH_3CH_2C(O)OH$	0.0/0.0	1.6	≤2	15^d	68^d	21^d	≤1.5	*nd*
methyl acetate	$CH_3C(O)OCH_3$	9.2/4646	1.9	22 ± 2	15 ± 2	68 ± 1	21^d	16 ± 3	*d*
anti-ethyl formate	*a*-$CH_3CH_2OC(O)H$	13.6/6820	2.2	1.82 ± 0.15	15^d	68^d	21^d	1.3 ± 0.2	*d*
gauche-ethyl formate	*g*-$CH_3CH_2OC(O)H$	13.9/7014	2.0	1.9 ± 0.2	15^d	68$^{(d)}$	21^d	1.4 ± 0.3	*td*
hydroxyacetone	$CH_3C(O)CH_2OH$	18.9/9510	3.3	2.11 ± 0.13	15^d	68^d	21^d	1.6 ± 0.2	*d*
lactaldehyde	$CH_3CH(OH)C(O)H$	23.8/11997	2.6	1.10 ± 0.13	15^d	68^d	21^d	0.81 ± 0.16	*fd*
3-hydroxypropanal	$HO(CH_2)_2C(O)H$	26.3/13239	3.0	0.86 ± 0.14	12^d	69^d	21$^{(d)}$	0.64 ± 0.14	*td*
methoxyacetaldehyde	$CH_3OCH_2C(O)H$	38.9/19581	3.0	0.33 ± 0.03	15^d	68^d	21^d	0.24 ± 0.04	*fd*
glycidol	c-CH_2OCHCH_2OH	51.0/25674	1.7	≤0.5	15^d	68^d	21^d	≤0.37	*nd*

Notes. [a] Relative energies (including ZPE corrections) and total electric dipole moments are computed at the B2PLYPD3/aug-cc-pVTZ level of theory (Grimme et al. 2011) using the Gaussian 16 program package (Frisch et al. 2016). [b] We adopted N_{H_2} = 1.35×10^{23} cm^{-2}, from Martín et al. (2008), assuming an uncertainty of 15% of its value. [c] Status of the search for each species toward G+0.693: *d* = detection, *fd* = first detection, *td* = tentative detection, and *nd* = non-detection. [d] Values fixed in the fit.

Sanz-Novo et al. 2025), and three C atoms such as propanol (C_3H_7OH; Jiménez-Serra et al. 2022) and 3-hydroxypropanal (Fried et al. 2025). The latter, which was tentatively detected earlier this year, motivated us to carry out the present follow-up study.

Our analysis has confirmed the presence of six additional $C_3H_6O_2$ isomers in G+0.693, including the first interstellar detection of lactaldehyde and methoxyacetaldehyde, together with the second interstellar detection (confirmation) of methyl acetate and hydroxyacetone and the fourth detection of ethyl formate in the ISM. Propionic acid and glycidol remain undetected, but we have also reported the upper limits of their molecular column densities, setting new constraints on their abundances in the ISM.

2. Observations

The astronomical search for the $C_3H_6O_2$ isomers was performed toward the GC molecular cloud G+0.693, located approximately 55" north-east of the well-known high-mass star-forming region Sgr B2(N). This source exhibits intermediate H_2 densities of 10^4–10^5 cm^{-3} that lead to the subthermal excitation of the molecular emission, with excitation temperatures between ~5–20 K (well below the kinetic temperature of the gas of 70–150 K; Requena-Torres et al. 2006; Zeng et al. 2018; Jiménez-Serra et al. 2020; Colzi et al. 2024). The spectra toward this source are, therefore, significantly less crowded than those observed toward hot cores, where some of the $C_3H_6O_2$ isomers have previously been detected and where vibrationally excited states are also efficiently populated. This considerably reduces the line blending and facilitates the identification of new interstellar species through a smaller number of rotational transitions.

In this study, we employed an ultra-deep spectral survey of this source that combines centimeter- and millimeter-wavelength observations acquired with two facilities. The *Q*-band range (31.075–50.424 GHz) was surveyed using the Yebes 40-m telescope in Guadalajara, Spain (projects 20A008 and 21A014), while the IRAM 30-m telescope in Granada, Spain, provided complementary coverage in two broadband millimeter-wavelength frequency windows (71.8–116.7 GHz, 124.8–175.5 GHz; see Rivilla et al. 2023; Sanz-Novo et al. 2023 and references therein; projects 172-18, 018-19, 133-19, 123-22). Data were collected in position-switching mode, centered at α = 17^{h}47^{m}22^s, δ = −28°21′27″ (J2000), with an off-source reference located at $\Delta\alpha$ = −885″ and $\Delta\delta$ = 290″. The Yebes telescope's half-power beam width (HPBW) spans ~55″–35″ from 31 to 50 GHz (Tercero et al. 2021), whereas the IRAM 30-m HPBW ranges from ~32″ to ~10″ across the targeted frequencies. Given that molecular emission toward G+0.693 is extended compared to the beam size of the telescope (Jones et al. 2012; Li et al. 2020; Zheng et al. 2024), we report all spectra in antenna temperature units (T_A^*). Overall, we achieved root-mean-square (rms) noise levels lying between 0.25 and 0.9 mK across the whole *Q* band, 0.5–2.5 mK at 3 mm, and 1.0–1.6 mK at 2 mm. Further details on these observations and their reduction are available in Rivilla et al. (2023) and Sanz-Novo et al. (2023).

3. Results

3.1. LTE analysis

We carried out a local thermodynamic equilibrium (LTE) analysis of all $C_3H_6O_2$ isomers for which rotational spectroscopic data are available using the Spectral Line Identification and Modeling (SLIM) tool (version from 15 June, 2024) within the MADCUBA software package (Martín et al. 2019). This tool allowed us to produce a synthetic spectrum of each target species and compare it directly with the observed spectra, as well as to evaluate the emission of all the molecules previously identified in the current molecular line survey (i.e., over 140 species).

To obtain the best-fit LTE model for each molecule, we used the AUTOFIT tool within SLIM (Martín et al. 2019) and performed a nonlinear least-squares LTE fit of a selected subset of clean transitions to the observed data using the Levenberg-Marquardt algorithm. We note that heavily blended lines, contaminated by the emission of previously identified species, were excluded from the analysis. For the fit, we can leave the following as free parameters: the molecular column density (N), the excitation temperature (T_{ex}), the radial velocity (v_{LSR}), and the line width (FWHM). As described in the following subsections, we fixed certain parameters for some of the studied species to that derived for the most abundant $C_3H_6O_2$ isomer, methyl acetate, which also presents the brightest transitions, to ensure convergence of the AUTOFIT.

In addition, to derive the fractional abundances with respect to molecular hydrogen for all targeted molecules, we adopted $N(H_2)$ = 1.35×10^{23} cm^{-2} from Martín et al. (2008), assuming an uncertainty of 15% of its value. For comparison and completeness, in Table 1 we list the physical parameters

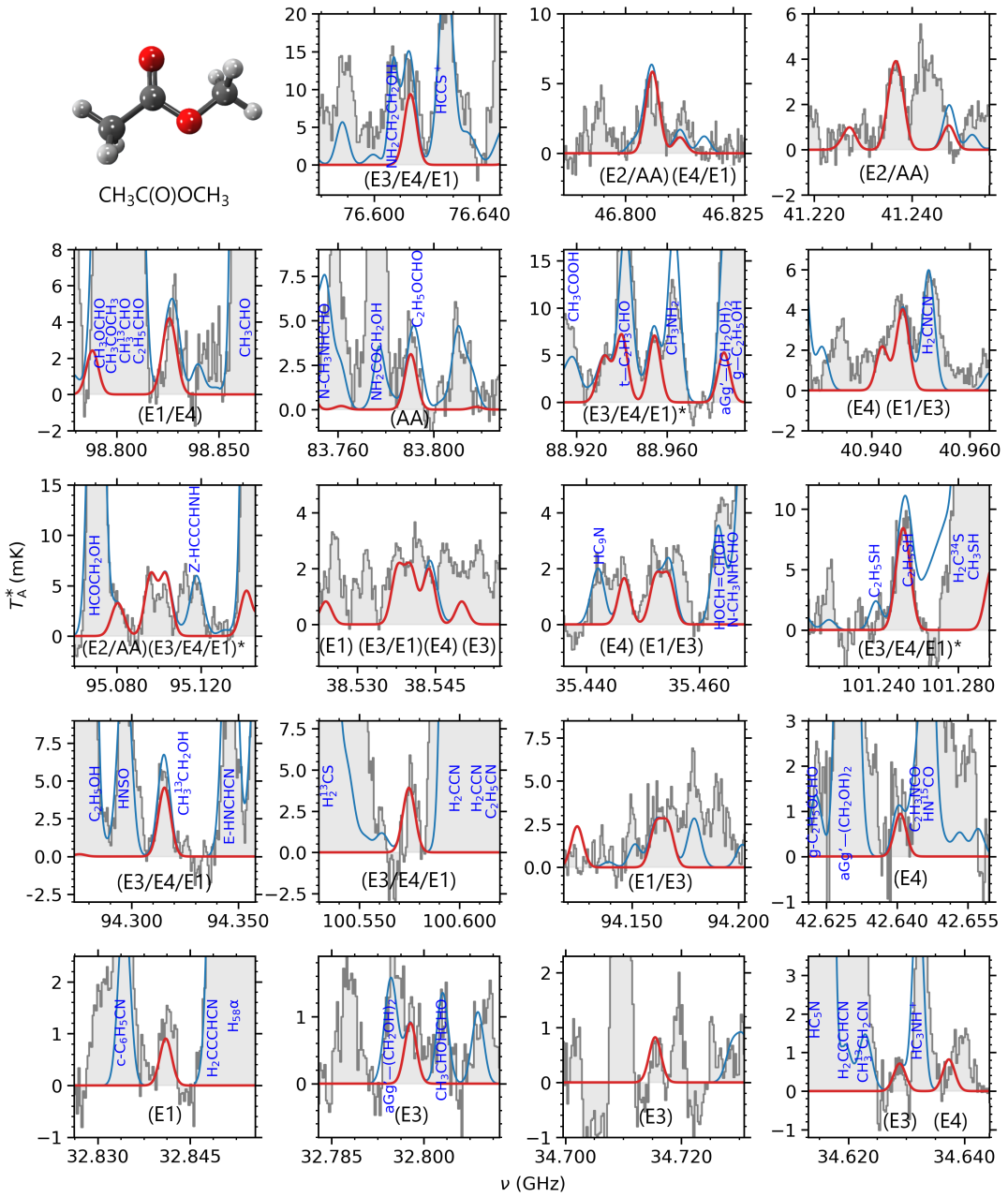

Fig. 2. Selected unblended or slightly blended transitions of methyl acetate, $CH_3C(O)OCH_3$, identified toward G+0.693, which were used to derive the LTE physical parameters of the molecule (see text; listed in Table A.1). The red line shows the best LTE fit of $CH_3C(O)OCH_3$, while the blue line represents the combined emission of all molecules identified in the survey (observed spectra are shown as gray histograms). The symmetry state of the detected transitions is shown at the bottom of each panel (full list of quantum numbers listed in Table A.1). The * symbol indicates that there are various transitions in the same panel, each comprising the same $E_3/E_4/E_1$ symmetry states. The transitions are sorted by decreasing intensity. The molecular structure of $CH_3C(O)OCH_3$ is also shown (C atoms in gray, O atoms in red, and H atoms in white).

derived for all $C_3H_6O_2$ isomers, including those reported for 3-hydroxypropanal in Fried et al. (2025).

3.2. Detection of methyl acetate

Methyl acetate, $CH_3C(O)OCH_3$, is the second most stable species within the $C_3H_6O_2$ isomeric family and was first detected in Orion KL by Tercero et al. (2013). However, this molecule has not yet been identified in any other astronomical environment. Here, we searched for $CH_3C(O)OCH_3$ toward G+0.693, which resulted in an unequivocal detection (see Figure 2), thus pointing to a broader presence of methyl acetate in the ISM. For the astronomical search, we employed the spectroscopic catalog derived from the original analysis using the BELGI-C_s-2Tops code (Tercero et al. 2013), which we converted into the common SPCAT/SPFIT format (Pickett 1991) (see Appendix A). This molecule exhibits two non-equivalent CH_3 internal rotors, which split the rotational energy levels into five substates (i.e., AA, AE, EA, and two EE species, E_3 and E_4, with statistical weights of 16, 16, 16, 8, and 8, respectively). In the transformed catalog, these symmetry species are labeled using the so-called vibrational quantum number as follows: 0 = AA, 1 = E_1 (EA), 2 = E_2 (AE), 3 = E_3 (EE), 4 = E_4 (EE) (see Table A.1).

In Figure 2, we show a selection of the brightest and least contaminated lines of $CH_3C(O)OCH_3$ that have been detected toward G+0.693, which were subsequently used to derive the physical parameters of the targeted molecular emission. Moreover, the fine structure corresponding to transitions belonging to the five symmetry states is, in some cases, partially resolved, giving rise to easily recognizable patterns, while in other cases it is fully merged into a single, broader spectral feature due to the typically broad line width of the molecular line emission measured toward G+0.693 (i.e., FWHM ~ 15–20 km s^{-1}; Requena-Torres et al. 2006, 2008; Zeng et al. 2018; Rivilla et al. 2022b). However, this "autoblending" likewise facilitates the detection because it strengthens the intensity of the resulting line cluster (e.g., $16_{1,16}$–$15_{1,15}$ transition at ~101.2512 GHz).

To yield the best LTE modeling for $CH_3C(O)OCH_3$, we used the AUTOFIT tool for the clean subset of transitions shown in Figure 2 (spectroscopic information reported in Table A.1). For the fit, we fixed the FWHM to a value of 21 km s^{-1}, which reproduces the brightest and cleanest transitions well, while the N, T_{ex} and v_{LSR} were left as free parameters. We obtained a $N = (2.2 \pm 0.2) \times 10^{14}$ cm^{-2}, which corresponds to a fractional abundance with respect to molecular hydrogen of $(1.6\pm 0.3) \times 10^{-9}$. Furthermore, we derived a $T_{ex} = 15 \pm 2$ K and a $v_{LSR} = 68 \pm 1$ km s^{-1}, consistent with those employed for the analysis of its isomer 3-hydroxypropanal (Fried et al. 2025) (see Table 1). We note that a change of 1–2 K in the T_{ex} only slightly affects the derived N, and in all cases this variation is smaller than the uncertainty assumed in the derivation of the fractional abundance with respect to H_2 (i.e., 15%).

3.3. Detection of anti-ethyl formate and tentative detection of gauche-ethyl formate

Next in energy, we find ethyl formate ($CH_3CH_2OC(O)H$). Its two lowest-in-energy conformers[1], *anti* and *gauche*, are separated by 65 ± 21 cm^{-1} (or 94 K; Riveros 1967) with the *anti* configuration being the global minimum in energy. The *anti* conformer (hereafter *a*-$CH_3CH_2OC(O)H$) has been detected in three hot molecular cores so far: Sgr B2(N), Orion KL, and W51 e2 (Belloche et al. 2009; Tercero et al. 2013; Rivilla et al. 2017; Peng et al. 2019), with the latter two sources also harboring *gauche* $CH_3CH_2OC(O)H$ (hereafter *g*-$CH_3CH_2OC(O)H$) in an approximately 1:1 abundance ratio.

In this work, we report a new detection of *a*-$CH_3CH_2OC(O)H$ toward G+0.693, while *g*-$CH_3CH_2OC(O)H$ is tentatively detected due to non-negligible line blending for the majority of lines (see Figures 3 and A.1). To perform the LTE analysis corresponding to the *a*-$CH_3CH_2OC(O)H$ emission, we used the spectroscopic catalog from the Cologne Database for Molecular Spectroscopy (CDMS, entry 074514; Endres et al. 2016), which is based on the laboratory data by Riveros (1967); Demaison et al. (1984); Medvedev et al. (2009). For the *g*-conformer, we employed a new spectroscopic entry using the aforementioned data, since the CDMS entry includes the rotational lines of *g*-$CH_3CH_2OC(O)H$ shifted by the corresponding $\Delta E(a\text{-}g)$; thus, they are not suitable for the analysis in regions whose molecular emission is well described by low excitation temperatures. Hence, we considered each conformer as distinct molecular species, as previously done for other molecules in G+0.693 (see, e.g., Jiménez-Serra et al. 2022; Sanz-Novo et al. 2023, 2025).

[1] Structures that share the same molecular formula and connectivity of atoms, but differ in their 3D arrangement in space.

After inspecting the astronomical data, various unblended or slightly blended *a*-type transitions ranging from $J = 6$ to $J = 9$, with $K_a < 3$ and belonging to *a*-$CH_3CH_2OC(O)H$ were detected. A selection of the brightest and cleanest transitions, which were subsequently used in the LTE fit with MADCUBA, are shown in Figure 3 (spectroscopic information reported in Table A.2). For completeness, we also show other transitions that appear blended, but their predicted intensities are nevertheless required to reproduce the observed spectra once the contribution of all species previously identified toward G+0.693 is taken into account. In this case, we fixed the T_{ex}, v_{LSR} and FWHM to the values derived for methyl acetate (i.e., $T_{ex} = 15$ K, $v_{LSR} = 68$ km s^{-1}, FWHM = 21 km s^{-1}), leaving the N as the only free parameter in the AUTOFIT. We derived a $N = (1.82 \pm 0.15) \times 10^{13}$ cm^{-2}, which yields a fractional abundance with respect to H_2 of $(1.3\pm0.2) \times 10^{-10}$.

Meanwhile, for *g*-$CH_3CH_2OC(O)H$ we detected two unblended lines along with seven additional lines showing slight blending. Therefore, the overall detection of this conformer remains tentative (see Figure A.1, spectroscopic information listed in Table A.3). Following the same fitting approach as for the *anti* conformer, we obtained a $N = (1.9 \pm 0.2) \times 10^{13}$ cm^{-2}, which corresponds to a fractional abundance with respect to H_2 of $(1.4 \pm 0.3) \times 10^{-10}$, and does not produce any overly bright feature for other transitions. Therefore, based on the derived abundance, we infer an *anti*/*gauche* ratio of 0.9±0.1, in excellent agreement with the ratio reported previously toward Orion KL and W51 e2 (of ~1; Tercero et al. 2013; Rivilla et al. 2017). Furthermore, the total abundance of $CH_3CH_2OC(O)H$ (i.e., the sum of the abundance of both *a*- and *g*-conformers) is a factor of 5.9±0.6 lower than that of $CH_3C(O)OCH_3$ in G+0.693, yielding a $CH_3C(O)OCH_3/CH_3CH_2OC(O)H$ abundance ratio, comparable to that observed previously toward Orion KL (of ~5; Tercero et al. 2013).

3.4. Detection of hydroxyacetone

To date, hydroxyacetone ($CH_3C(O)CH_2OH$; the fourth most stable structural isomer) has only been detected toward the protostar IRAS 16293–2422B (Zhou et al. 2020). We conducted a new search for the molecule toward G+0.693, yielding the second interstellar detection (first one outside a hot core) and confirming its presence in the ISM.

To carry out the search, we used the spectroscopic entry of the ground vibrational state of $CH_3C(O)CH_2OH$ included in the Jet Propulsion Laboratory (JPL) database (entry 74003; Pickett et al. 1998) based on high-resolution microwave, millimeter- and submillimeter-wave laboratory data by Braakman et al. (2010). The molecule presents a low barrier CH_3 internal rotor, which causes the splitting of the energy levels into the A and E symmetry states. In this case, we detected several nearly complete progressions of *R*-branch *a*-type transitions ranging from $J = 5$ to $J = 8$ (a total of six fully unblended lines), with $K_a = 0,1$ and belonging to $CH_3C(O)CH_2OH$, along with few additional higher K_a lines (see Figure 4, spectroscopic information reported in Table A.4). To conduct the LTE analysis, we again left the N as the only free parameter and fixed the rest of the parameters to those obtained for methyl acetate (listed in Table 1). We retrieved a $N = (2.11 \pm 0.13) \times 10^{13}$ cm^{-2}, which translates into a fractional abundance with respect to H_2 of $(1.6\pm 0.2) \times 10^{-10}$. Based on the derived abundance, $CH_3C(O)CH_2OH$ is a factor of 10±1 less abundant than $CH_3C(O)OCH_3$, and 1.8±0.1 times less abundant than $CH_3CH_2OC(O)H$.

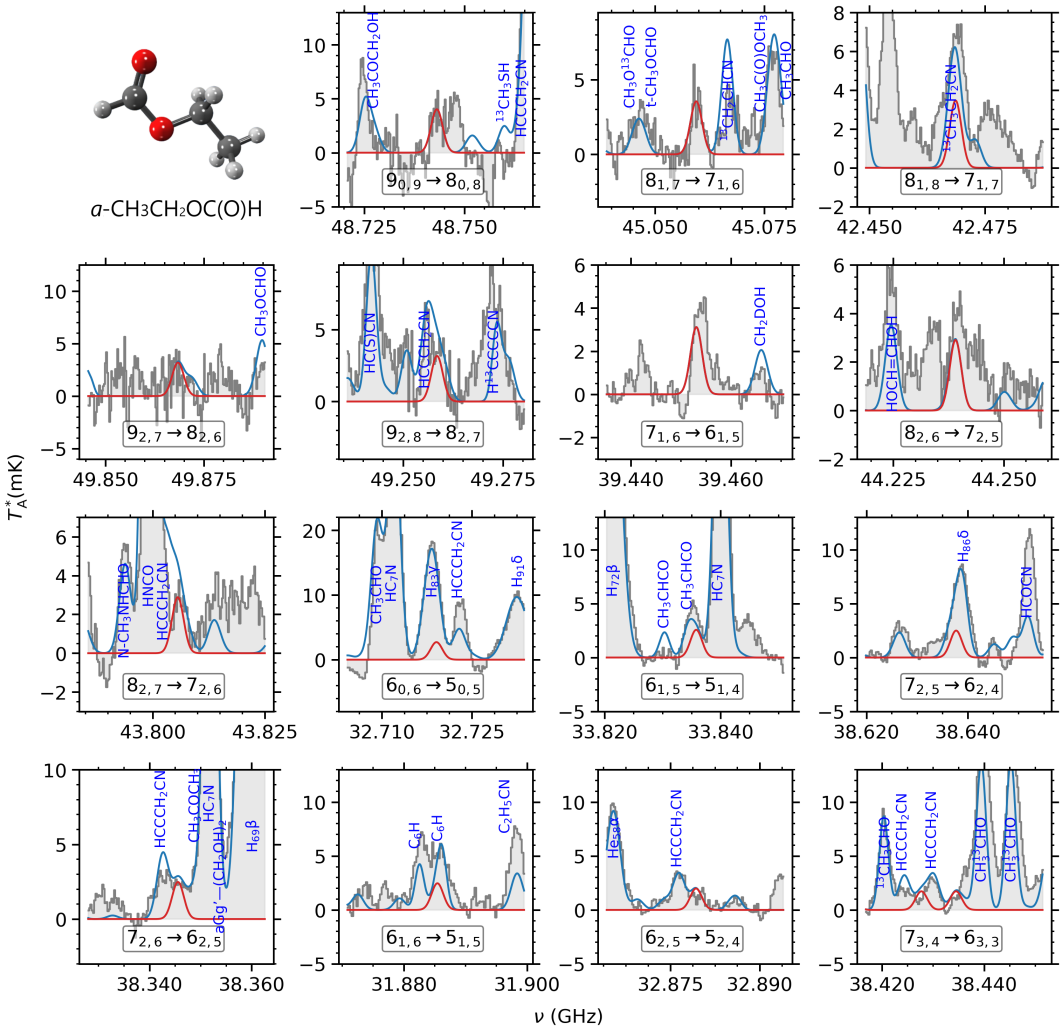

Fig. 3. Transitions of *a*-ethyl formate, *a*-$CH_3CH_2OC(O)H$, identified toward G+0.693, which were used to derive the LTE physical parameters of the molecule (see text; listed in Table A.2). The red line shows the best LTE fit of *a*-$CH_3CH_2OC(O)H$, while the blue line represents the combined emission of all molecules identified in the survey, including *a*-$CH_3CH_2OC(O)H$ (observed spectra are shown as gray histograms). The quantum numbers for each transition are shown at the bottom of each panel. The transitions are sorted by decreasing intensity. The molecular structure of *a*-$CH_3CH_2OC(O)H$ is also shown (C atoms in gray, O atoms in red, and H atoms in white).

3.5. Detection of lactaldehyde

For lactaldehyde (2-hydroxypropanal, $CH_3CH(OH)C(O)H$; ranked as the fifth most stable structural isomer), we incorporated the high-resolution rotational data collected by Alonso et al. (2019) into MADCUBA, which corresponds to entry 074519 from CDMS (Endres et al. 2016). The exquisite sub-mK sensitivity of the present spectral survey toward G+0.693 allowed us to detect three clear and clean emission features that could be unambiguously ascribed to the $5_{0,5}$–$4_{1,4}$, $6_{0,6}$–$5_{1,5}$ and $6_{1,6}$–$5_{0,5}$ transitions of $CH_3CH(OH)C(O)H$ (see Figure 5, spectroscopic information reported in Table A.5). These correspond to the brightest K_a = 0,1 *R*-branch *b*-type transitions that fall within the ultra-deep *Q*-band data, all of which appear free of blending and exhibit good integrated signal-to-noise (S/N) ratios (S/N = 12, 16, and 18, respectively; rms = 0.37 mK, 0.34 mK, and 0.43 mK)[2]. We also detected the adjacent $7_{0,7}$–$6_{1,6}$ transition, as well as a few additional higher K_a lines that appear blended but reproduce the observed spectra well once the contribution from all other identified species is considered (solid blue line). We note that $CH_3CH(OH)C(O)H$ is a near-prolate asymmetric top, exhibiting a dominant *b*-type spectrum (μ_a = 1.1 D, μ_b = 2.2 D, μ_c = 0.93; computed at the B2PLYPD3-aug-cc-pVTZ level). The fact that A ≫ B, C implies that the strongest *R*-branch *b*-type progressions (e.g., $J'_{1,J'} \rightarrow J''_{0,J''}$, which appear at frequencies close to $A + C + 2CJ''$) are shifted toward higher frequencies compared to the *a*-type *R*-branch lines detected for other isomers, which occur near $(B + C)(J'' + 1)$. Consequently, fewer intense transitions of $CH_3CH(OH)C(O)H$ are expected within the *Q* band, where the sensitivity is the highest (see Rivilla et al. 2023; Sanz-Novo et al. 2023; Sanz-Novo et al. 2025). Accordingly, only a few unblended or slightly blended transitions are detected at higher frequencies (e.g., 3 mm window; see last row of Figure 5), and the rest appear either heavily blended or the derived S/N is significantly lower. Nevertheless, in all cases the LTE model is consistent with the observed spectra, and we note that no missing lines of $CH_3CH(OH)C(O)H$ are detected across the entire survey.

[2] The S/N is calculated from the integrated signal ($\int T_A^* dv$) and noise level σ = rms × $\sqrt{\delta v \times \mathrm{FWHM}}$, where δv is the velocity resolution of the spectra and the FWHM is fit from the data (i.e., 21 km s^{-1}).

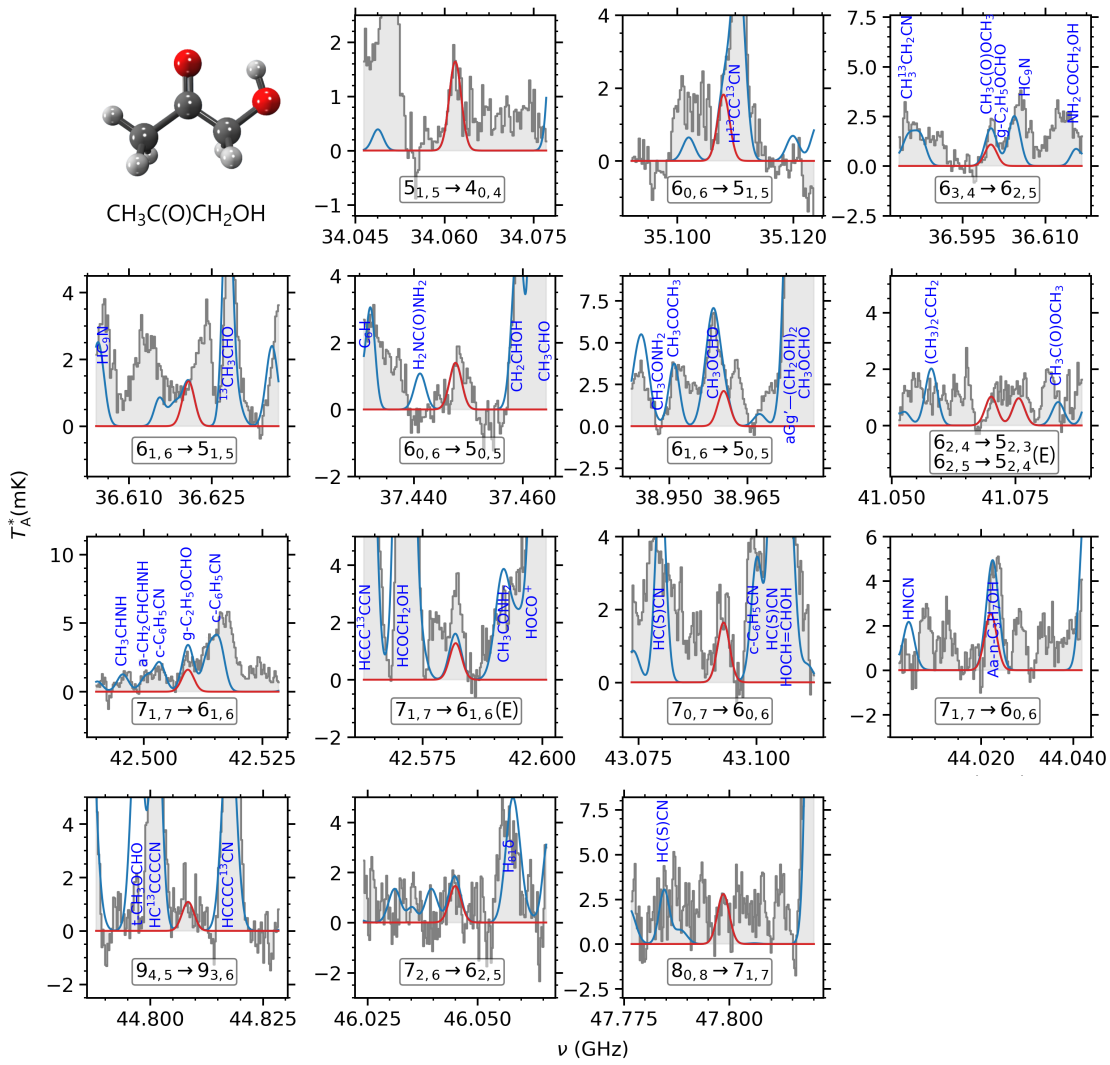

Fig. 4. Transitions of hydroxyacetone, $CH_3C(O)CH_2OH$, detected toward G+0.693 (see text; listed in Table A.4). The red line shows the best LTE fit of $CH_3C(O)CH_2OH$, while the blue line represents the combined emission of all molecules identified in the survey, including $CH_3C(O)CH_2OH$ (observed spectra are shown as gray histograms). The quantum numbers for each transition are shown at the bottom of each panel (A-state lines unless stated otherwise). The transitions are sorted by increasing frequency. The molecular structure of $CH_3C(O)CH_2OH$ is also shown (C atoms in gray, O atoms in red, and H atoms in white).

Following the same fitting approach as described above for other isomers, the AUTOFIT analysis yielded a $N = (1.10 \pm 0.13) \times 10^{13}$ cm^{-2}, which translates into an abundance of $(8.1 \pm 1.6) \times 10^{-11}$. Accordingly, we find that lactaldehyde is 20±3, 3.4±0.4, and 1.9±0.2 times less abundant than methyl acetate, ethyl formate, and hydroxyacetone, respectively, and is only slightly more abundant (a factor of 1.3±0.2) than its positional isomer 3-hydroxypropanal in G+0.693 (Fried et al. 2025).

3.6. Detection of methoxyacetaldehyde

Methoxyacetaldehyde ($CH_3OCH_2C(O)H$) has previously been searched for, without success, toward Orion KL and Sgr B2, as well as toward the dark cloud Barnard 1 (Kolesniková et al. 2018). To perform the astronomical search, we implemented the spectroscopic entry into MADCUBA (CDMS entry 074517 Endres et al. 2016, based on Kolesniková et al. 2018). Although $CH_3OCH_2C(O)H$ also presents methyl internal rotation, its V_3 barrier is higher than that of methyl acetate, and the A/E splittings were not resolved at 3mm with a conventional absorption spectrometer (Kolesniková et al. 2018) or with the resolution of the present survey (Rivilla et al. 2023; Sanz-Novo et al. 2023).

An inspection of the data of G+0.693 revealed a clear pattern of *R*-branch *a*-type transitions belonging to $CH_3OCH_2C(O)H$ (see Figure 6). Among these, the $8_{1,8}$–$7_{1,7}$, $9_{1,9}$–$8_{1,8}$ and $9_{0,9}$–$8_{0,8}$ transitions are fully unblended and show a good integrated S/N ratio (S/N = 12, 14, and 14, respectively; rms = 0.44 mK, 0.48 mK, and 0.48 mK). We also identified the $8_{0,8}$–$7_{0,7}$, $9_{2,7}$–$8_{2,6}$, and $10_{1,10}$–$9_{1,9}$ transitions, which are slightly contaminated with $^{13}CH_2CHCN$ and two U-lines, respectively, as well as a few additional K_a = 0, 1, and 2 transitions that appear more blended. Nevertheless, all these transitions help to reproduce the observations once the emission from all other molecules previously identified toward G+0.693 are taken into account, further reinforcing the detection. The spectroscopic information of all these transitions is reported in Table A.6. We then used the aforementioned unblended and slightly blended transitions of $CH_3OCH_2C(O)H$ to carry out the LTE analysis. We retrieved a $N = (3.3 \pm 0.3) \times 10^{12}$ cm^{-2} with the AUTOFIT tool. This corresponds to a fractional abundance with respect to H_2 of

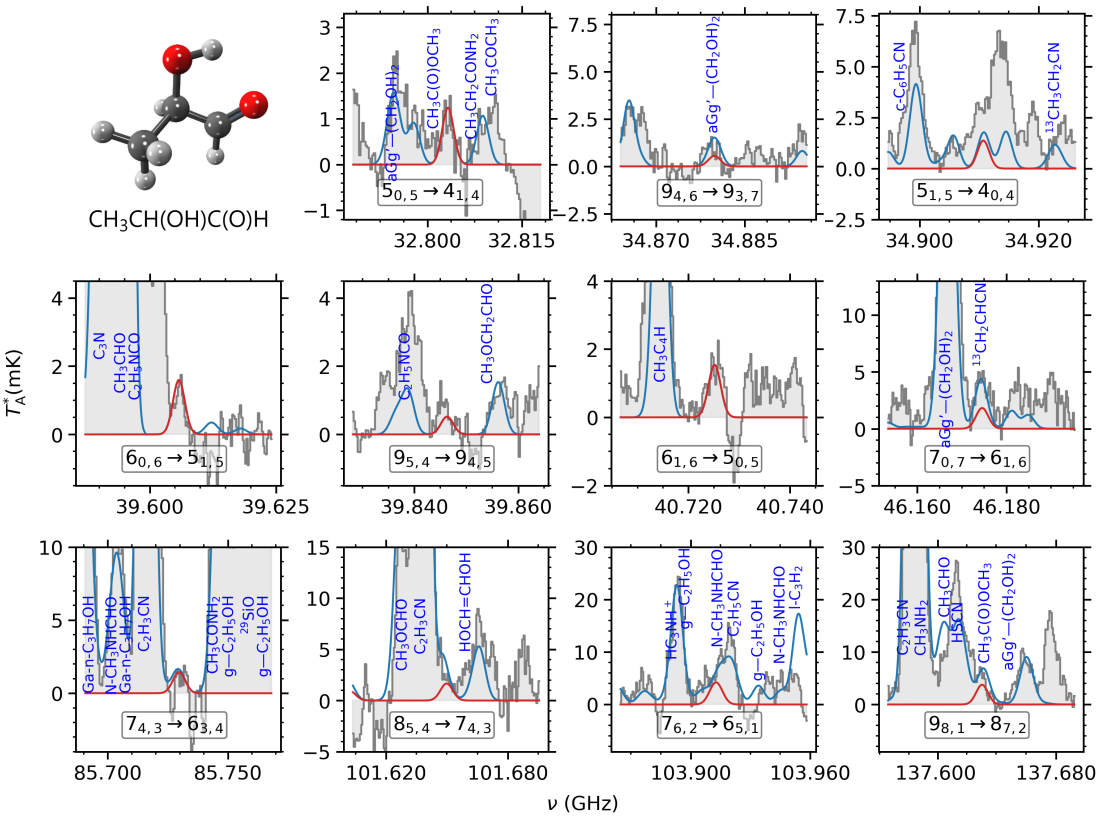

Fig. 5. Transitions of lactaldehyde, $CH_3CH(OH)C(O)H$, identified toward G+0.693 (see text; listed in Table A.5). The red line shows the best LTE fit of $CH_3CH(OH)C(O)H$, while the blue line represents the combined emission of all molecules identified in the survey, including $CH_3CH(OH)C(O)H$ (observed spectra are shown as gray histograms). The quantum numbers for each transition are shown at the bottom of each panel. For panels with multiple lines, we show the quantum number of the lowest-frequency transition. The transitions are sorted by increasing frequency. The molecular structure of $CH_3CH(OH)C(O)H$ is also shown (C atoms in gray, O atoms in red, and H atoms in white).

$(2.4 \pm 0.4) \times 10^{-11}$. Consequently, $CH_3OCH_2C(O)H$ shows the lowest abundance among all $C_3H_6O_2$ isomers, that is, a factor of 67±9, 11±1, 6.4±0.7, 3.3±0.4, and 2.6±0.5 less abundant than methyl acetate, ethyl formate, hydroxyacetone, lactaldehyde, and 3-hydroxypropanal, respectively, in G+0.693.

3.7. Non-detection of propionic acid and glycidol

Propionic acid, $CH_3CH_2C(O)OH$, besides being the most thermodynamically favored $C_3H_6O_2$ isomer, also exhibits the lowest total dipole moment within this molecular family (i.e., μ_a = 0.2 D, μ_b = 1.6 D; computed at the B2PLYPD3-aug-cc-pVTZ level). It has previously been searched for toward Orion KL and Sgr B2(N) (Ilyushin et al. 2021); however, the molecule remains undetected. Here, we searched for $CH_3CH_2C(O)OH$ toward G+0.693 using a catalog based on the spectroscopy reported in Jaman et al. (2015), but we did not achieve a detection. Although many transitions still leave room for the possible presence of the molecule, the majority of the brightest transitions are affected by significant line blending (see Figure A.2). To derive the upper limits for its column density, we fixed the T_{ex}, v_{LSR}, and FWHM to that of methyl acetate (listed in Table 1) and increased N until the LTE model (including also the contribution from other species) visually matched the observed spectra for the brightest K_a = 1 transition, $8_{1,8}$–$7_{0,7}$ (at 49.3424 GHz). We estimated a $N \leq 2 \times 10^{13}$ cm^{-2}, which yields a fractional abundance with respect to H_2 of $\leq 1.5 \times 10^{-10}$.

We also targeted the cyclic species glycidol (c-CH_2OCHCH_2OH), which, to our knowledge, has not been searched for in the ISM to date. We used a newly generated catalog in SPFIT/SPCAT format, based on the spectroscopic parameters reported by Demaison et al. (2012), and implemented it into MADCUBA. After analyzing the data, we did not detect any bright, unblended transition of c-CH_2OCHCH_2OH (see Figure A.3). We note that this species presents a relatively low total dipole moment (i.e., the second lowest after $CH_3CH_2C(O)OH$; μ_a = 0.7 D, μ_b = 1.3 D, μ_c = 0.8 D, computed at the B2PLYPD3-aug-cc-pVTZ level), which will hamper its detection. To derive the line-integrated 3σ upper limit to its column density (σ being the rms noise of the spectra), we used the $5_{5,1}$–$4_{4,0}$ and $5_{5,0}$–$4_{4,1}$ transitions (fully coalesced and located at ~97.0723 GHz), which is the brightest feature predicted for c-CH_2OCHCH_2OH, only negligibly blended with $CH_3(O)OCH_3$. We obtained a $N \leq 0.5 \times 10^{13}$ cm^{-2}, which translates into an abundance upper limit of $\leq 3.7 \times 10^{-11}$.

4. Astrochemical implications and conclusions

The detection of six distinct $C_3H_6O_2$ structural isomers toward G+0.693 (i.e., methyl acetate, hydroxyacetone, ethyl formate, 3-hydroxypropanal, lactaldehyde, and methoxyacetaldehyde), together with the non-detection of propionic acid and glycidol, allows us to delve further into the formation of these species in the ISM.

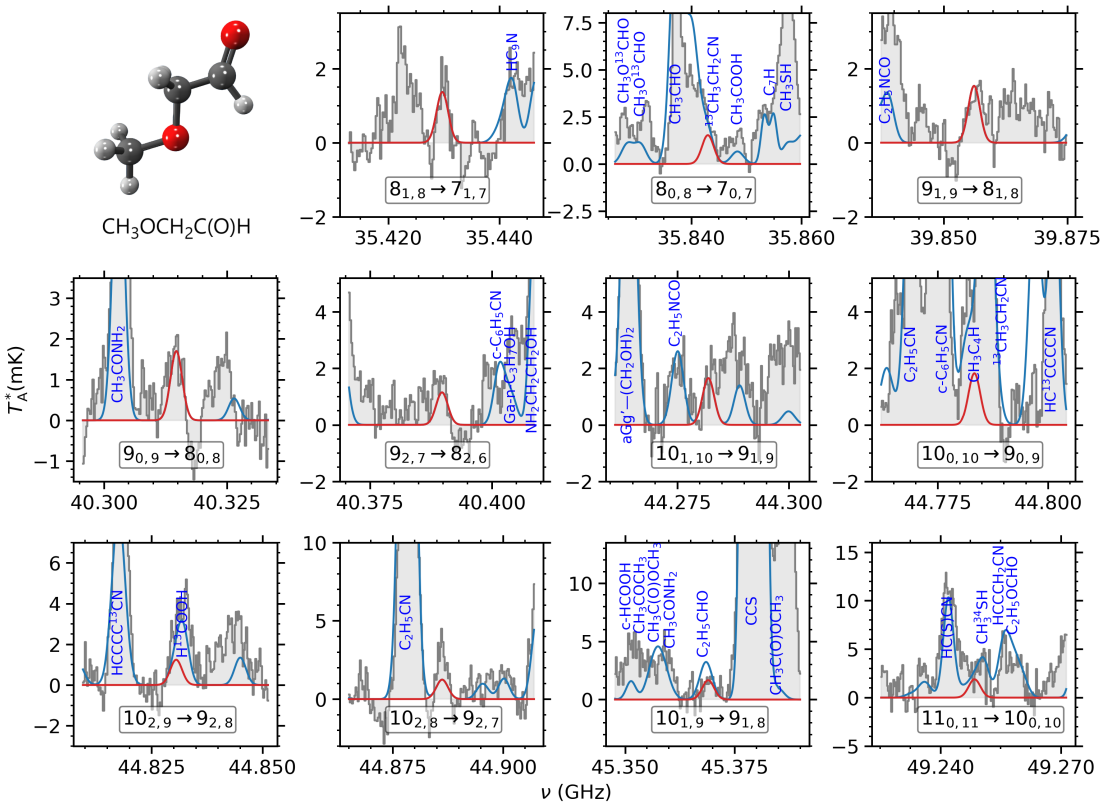

Fig. 6. Transitions of methoxyacetaldehyde, $CH_3OCH_2C(O)H$, detected toward G+0.693 (collected in Table A.6). The red line shows the best LTE fit of $CH_3OCH_2C(O)H$, while the blue line represents the combined emission of all molecules identified in the survey, including $CH_3OCH_2C(O)H$ (observed spectra are shown as gray histograms). The quantum numbers for each transition are shown at the bottom of each panel. The transitions are sorted by increasing frequency. The molecular structure of $CH_3OCH_2C(O)H$ is also shown (C atoms in gray, O atoms in red, and H atoms in white).

Here, we focus on possible grain-surface chemical formation pathways, which have previously been demonstrated to produce multiple $C_3H_6O_2$ isomers upon UV irradiation of methanol–acetaldehyde and CO–ethanol ices (Wang et al. 2023; Wang et al. 2024). As shown in Figure 7, all the proposed routes proceed through a final radical–radical recombination reaction starting from the parent molecule CO, which can either be hydrogenated to form methanol (CH_3OH; Jiménez-Serra et al. 2025) or oxygenated to yield HOCO and, eventually, CO_2 (Garrod & Pauly 2011; Minissale et al. 2013; Molpeceres et al. 2025). In the former case, CH_3OH can undergo H-abstraction to produce the CH_2OH and CH_3O radicals, which may subsequently react with CH_3CO and $CH_2C(O)H$ to form hydroxyacetone, 3-hydroxypropanal, methyl acetate, and methoxyacetaldehyde, although to our knowledge the latter has not been detected in previous experiments (Wang et al. 2023; Wang et al. 2024). Alternatively, CH_3OH can evolve into CH_3CH_2OH, which, upon H-abstraction, yields CH_3CH_2O, CH_2CH_2OH, or CH_3CHOH, depending on the abstraction site. These radicals can then react with the H(O)C radical, thought to form efficiently via hydrogenation of CO (Brown et al. 1988) or H-abstraction from formaldehyde ($H_2(O)C$), leading to the formation of ethyl formate, 3-hydroxypropanal, and lactaldehyde, respectively. Remarkably, lactaldehyde has been proposed as a key building block for relevant prebiotic molecules, such as pyruvic acid, methylglyoxal, and lactic acid, which participate in the methylglyoxal cycle and are considered as precursors of amino acids, sugars, and sugar acids (Wang et al. 2024).

While the formation routes described above could indeed account for the formation of the targeted $C_3H_6O_2$ isomers in the ISM, their efficiency depends critically on two ingredients: (i) a high cosmic-ray ionization rate (CRIR) to promote radical–radical recombination reactions, and (ii) access to the chemistry that occurs on the surface of dust grains, enabled by the desorption of ice-mantle species into the gas phase. This aligns perfectly with two of the key factors driving the exceptionally rich chemistry observed in G+0.693. First, large-scale, low-velocity shocks, likely resulting from a cloud–cloud collision scenario (Requena-Torres et al. 2006; Zeng et al. 2020; Colzi et al. 2024), enhance the sputtering of icy grain mantles, thereby exposing surface chemistry. Second, the high CRIR that is thought to affect the cloud (10^{-14}–10^{-15} s^{-1}), inferred from chemical modeling of the PO^+ and $HOCS^+$ cations (Rivilla et al. 2022b; Sanz-Novo et al. 2024), has been suggested to facilitate the formation of radicals on these icy mantles. Once generated, these radicals can efficiently interact and recombine, ultimately driving the synthesis of increasingly complex molecules (Rivilla et al. 2023).

On a different note, the non-detection of propionic acid and glycidol provides additional valuable information. These species exhibit the lowest dipole moments among all isomers (see Figure 1), which significantly hampers their astronomical detection. Interestingly, while most $C_3H_6O_2$ isomers can be formed through the hydrogenation of CO (Figure 7), propionic acid follows a distinct chemical route. Its formation begins with the oxygenation of CO via the reaction CO + OH, producing

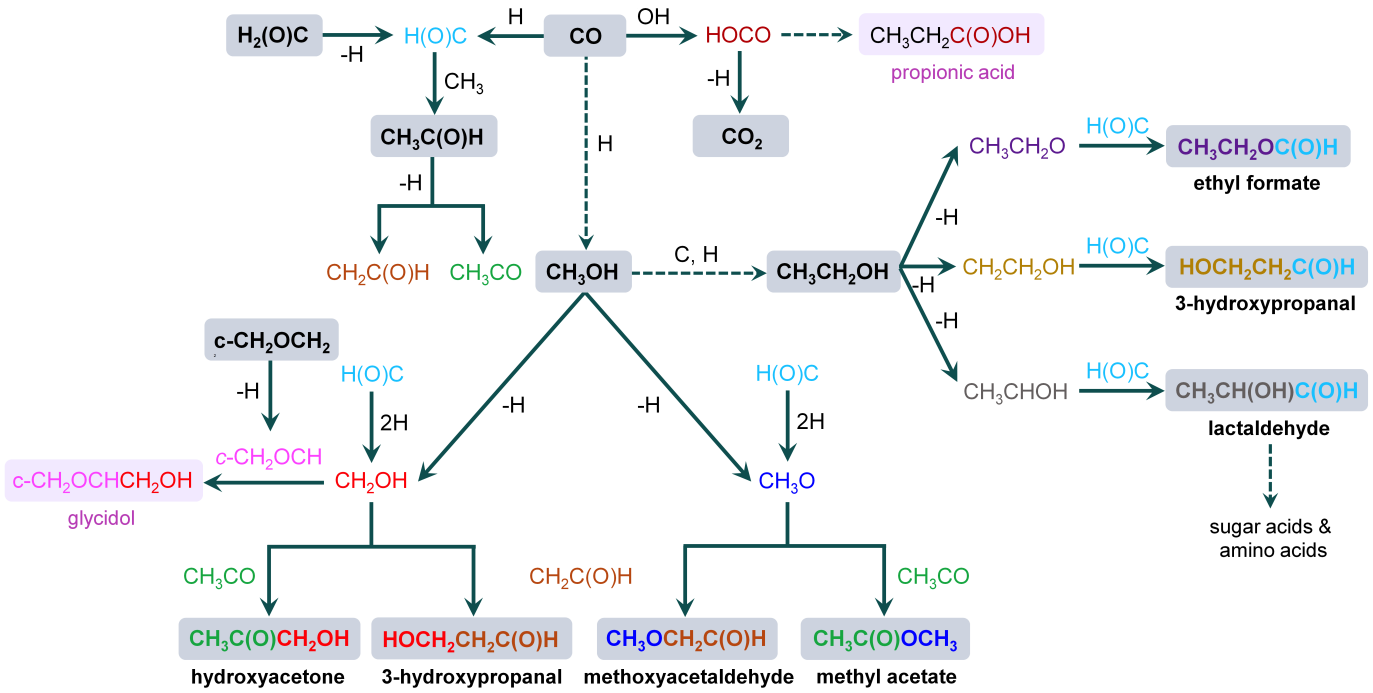

Fig. 7. Suggested grain-surface chemical routes for the formation of targeted $C_3H_6O_2$ isomers in the ISM. Dashed lines indicated processes involving more than one step. We highlight in boldface molecules identified toward G+0.693. $C_3H_6O_2$ species that were not detected and whose formation has not been tested experimentally by Wang et al. (2023) and Wang et al. (2024) are highlighted with a light purple box. For simplicity, stereoisomerism is not considered in this plot.

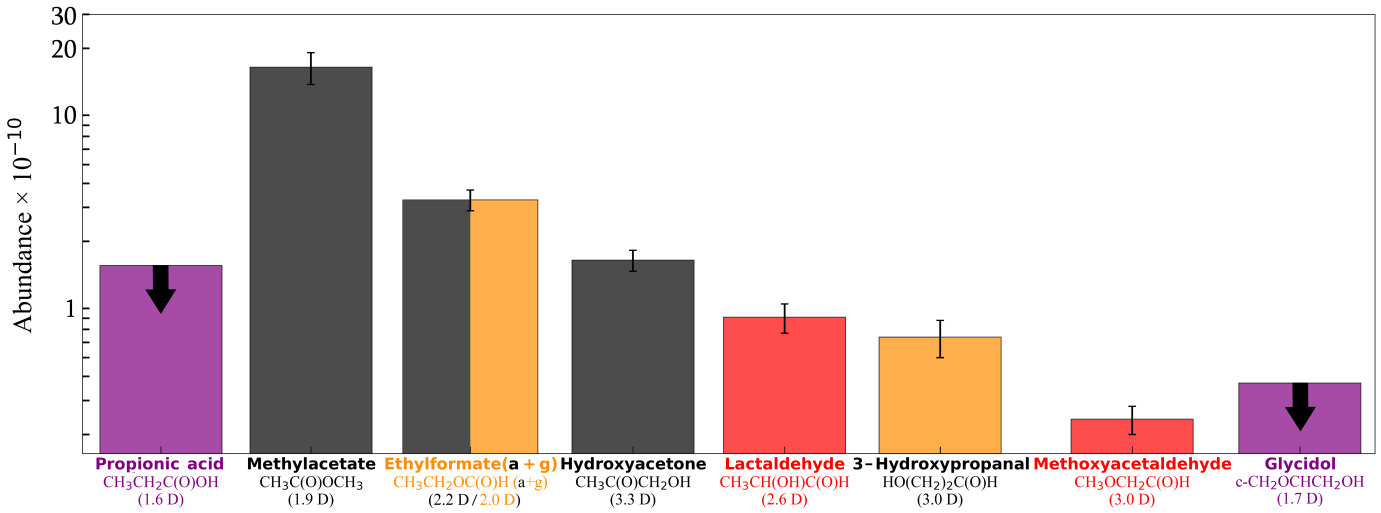

Fig. 8. Fractional abundances with respect to H_2 of different $C_3H_6O_2$ isomers sorted by increasing relative energy. The total dipole moment for each molecule (computed at the B2PLYP-D3/aug-cc-pVTZ level) is included. We used the same color-code as that in Fig. 1: new first detections in the ISM are shown in red, tentative detections in orange, non-detections in purple (upper limits indicated with black arrows), and previous detections toward different sources in black.

the HOCO radical, which is widely considered a key precursor in the formation of interstellar carboxylic acids (see, e.g., Oba et al. 2010; Ioppolo et al. 2021; Ishibashi et al. 2024; Molpeceres et al. 2025). This species can either be converted into CO or CO_2 (Molpeceres et al. 2025) or, alternatively, it could lead to the formation of more complex acids such as propionic acid. However, this latter pathway might represent only a minor channel, given the limited reservoir of complex carboxylic acids currently known in the ISM (Sanz-Novo et al. 2023). Furthermore, the chemical distinction proposed here between propionic acid and the other $C_3H_6O_2$ isomers is consistent with the spatial differentiation observed in ALMA interferometric observations toward Orion KL by Tercero et al. (2018), which is clearly differentiated for methyl acetate and ethyl formate compared to that of the carboxylic acids (HCOOH and CH_3COOH).

At this point, we can compare the upper limit to the column density derived for propionic acid with the abundance of the related *trans*-formic acid (*t*-HCOOH; $N = (2.0 \pm 0.4) \times 10^{14}$ cm^{-2}) and acetic acid (CH_3COOH; $N = (4.5 \pm 0.2) \times 10^{13}$ cm^{-2}), both of which are also detected toward G+0.693

(Sanz-Novo et al. 2023). As has been observed for other chemical families such as alcohols, thiols, aldehydes, and isocyanates (Rodríguez-Almeida et al. 2021a,b; Jiménez-Serra et al. 2022; Sanz-Novo et al. 2022; Fried et al. 2025), the abundances typically decrease by roughly one order of magnitude with increasing molecular complexity (i.e., the substitution of a $–CH_3$ group). In this case, the observed ratios are *t*-$HCOOH/CH_3COOH$ = 4.4 ± 0.9 and $CH_3COOH/CH_3CH_2COOH \geq 2.0$, which suggests that we may still be below the sensitivity level required to detect CH_3CH_2COOH.

Regarding glycidol, while the proposed formation route also begins with CH_3OH, it requires an additional precursor for the suggested radical–radical recombination reaction: *c*-CH_2OCH. This radical could be produced via H-abstraction of ethylene oxide (*c*-CH_2OCH_2). However, the relatively low abundance of *c*-CH_2OCH_2 observed toward G+0.693 ($N \sim 10^{14}$ cm^{-2}; fractional abundance of $\sim 7 \times 10^{-10}$; Requena-Torres et al. 2008) compared with the other precursors such as CH_3OH and CH_3CH_2OH, which are ∼2 and ∼1 orders of magnitude more abundant than *c*-CH_2OCH_2, respectively (i.e., $1.1\pm0.2 \times 10^{-7}$ and $4.6\pm0.6 \times 10^{-9}$; Rodríguez-Almeida et al. 2021a), may hamper the detection of glycidol in the present survey. Additionally, we highlight that neither glycidol nor propionic acid were found in the experiments by Wang et al. (2023); Wang et al. (2024).

Finally, the comparison of the abundances of the detected $C_3H_6O_2$ isomers (Table 1) leads to the following ordering (see Figure 8):

N(methyl acetate) > *N*(ethyl formate) > *N*(hydroxyacetone) > *N*(lactaldehyde) > *N*(3-hydroxypropanal) > *N*(methoxyacetaldehyde).

Methyl acetate clearly emerges as the dominant isomer within the $C_3H_6O_2$ family, followed by ethyl formate and hydroxyacetone. Surprisingly, the observed abundance trend qualitatively follows the relative thermodynamic stability of the detected isomers (Figure 8). However, a major exception is propionic acid, the most stable member of the family, which remains undetected. This discrepancy shows that thermodynamic stability alone cannot be used as a reliable tool to predict the molecular abundances within this isomeric family in the ISM, as reported for other families (e.g., C_3H_2O, $C_2H_4O_2$, $C_2H_2N_2$, and $C_2H_5NO_2$; Loomis et al. 2015; Mininni et al. 2020; Shingledecker et al. 2020; Rivilla et al. 2023; San Andrés et al. 2024). Instead, kinetics are likely responsible for distinguishing among species arising from separated chemical formation pathways (i.e., those originating from CH_3OH or from HOCO; see Figure 7).

On the other hand, the significantly higher abundance of methyl acetate may suggest that the formation of this species is more efficient, potentially due to additional formation pathways occurring either on dust grains or in the gas phase (e.g., Das et al. 2015). Alternatively, if the relative dipole principle (RDP; Shingledecker et al. 2020) applies to this isomeric family, then the lower dipole moment of methyl acetate (μ_{tot} = 1.9 D, see Table 1) would lead to a slower destruction in the gas phase compared to the other detected species. Nevertheless, further theoretical, laboratory, and modeling effort is needed to shed conclusive light on this question.

In summary, our systematic survey of all $C_3H_6O_2$ isomers toward G+0.693 has significantly expanded the census of complex organic molecules in the ISM, particularly within this isomeric family. We report the interstellar discovery of lactaldehyde and methoxyacetaldehyde, along with the confirmation of methyl acetate and hydroxyacetone, and new detections in G+0.693 of both *anti*- and *gauche*-conformers of ethyl formate. These results not only enhance our understanding of the molecular inventory in the ISM, but also emphasize the importance of highly sensitive spectral line surveys for detecting the less-abundant species. Furthermore, they provide a rationale for the more than decade-long gap between the detection of methyl acetate and ethyl formate and the new interstellar discoveries reported in this work. These results also underscore the need for future laboratory and observational efforts targeting other uncharacterized $C_3H_6O_2$ isomers, including various enol tautomers (e.g., prop-1-ene-1,2-diol, prop-2-ene-1,2-diol, 1-methoxyethen-1-ol, prop-1-ene-1,3-diol) proposed by Wang et al. (2023), which may be efficiently produced via keto–enol tautomerization. Based on our findings, these species also appear as promising candidates for future interstellar detection.

Acknowledgements. We are grateful to the IRAM 30 m and Yebes 40 m telescopes staff for their help during the different observing runs, highlighting project 21A014 (PI: Rivilla), project 018-19 (PI: Rivilla) and projects 123-22 and 076-23 (PI: Jiménez-Serra). The 40 m radio telescope at Yebes Observatory is operated by the Spanish Geographic Institute (IGN, Ministerio de Transportes, Movilidad y Agenda Urbana). IRAM is supported by INSU/CNRS (France), MPG (Germany) and IGN (Spain). M.S.-N. acknowledges a Juan de la Cierva Postdoctoral Fellow proyect JDC2022-048934-I, funded by the Spanish Ministry of Science, Innovation and Universities/State Agency of Research MICIU/AEI/10.13039/501100011033 and by the European Union "NextGenerationEU"/PRTR". V.M.R. acknowledges support from the grant RYC2020-029387-I funded by MICIU/AEI/10.13039/501100011033 and by "ESF, Investing in your future". V.M.R., A.L-G. and D.S.A from the Consejo Superior de Investigaciones Científicas (CSIC) and the Centro de Astrobiología (CAB) through the project 20225AT015 (Proyectos intramurales especiales del CSIC), and from the grant CNS2023-144464 funded by MICIU/AEI/10.13039/501100011033 and by "European Union NextGenerationEU/PRTR". I.J.-S., V.M.R., M.S.-N, L.C., A.M., D.S.A, A.L-G. and A.M.-H. acknowledge funding from grant No. PID2022-136814NB-I00 from MICIU/AEI/10.13039/501100011033 and by "ERDF, UE". I.J.-S. and A.M. also acknowledge funding from the ERC grant OPENS (project number 101125858) funded by the European Union. Views and opinions expressed are however those of the author(s) only and do not necessarily reflect those of the European Union or the European Research Council Executive Agency. Neither the European Union nor the granting authority can be held responsible for them. D.S.A. also extends his gratitude for the financial support provided by the Comunidad de Madrid through the Grant PIPF-2022/TEC-25475. A.M.-H. acknowledges funding from grant MDM-2017-0737 Unidad de Excelencia "María de Maeztu" Centro de Astrobiología (CAB, CSIC-INTA) funded by MICIU/AEI/10.13039/501100011033. B.A.M. and Z.T.P.F. acknowledge support from Schmidt Family Futures. L.K. acknowledges financial funding from the Czech Science Foundation (GACR, grant No. 24-12586S). B.T. acknowledges Spanish Ministry of Science support from grants PID2022-137980NB-I00 and PID2023-147545NB-I00. J.-C.G. thanks the Centre National d'Etudes Spatiales (CNES) for a grant and the Programme National "Physique et Chimie du Milieu Interstellaire" (PCMI) of CNRS/INSU with INC/INP co-funded by CEA and CNES. E.J.C. acknowledges financial support from the Spanish Ministry of Science and Innovation (MCIN/AEI, Project PID2023-147698NB-I00) and the Basque Government (Project IT1491-22) I.K. would like to thank the Agence Nationale de la recherche Scientifique (ANR) project ANR-25-CE29-7779.

References

Alonso, E. R., McGuire, B. A., Kolesniková, L., et al. 2019, ApJ, 883, 18
Belloche, A., Garrod, R. T., Müller, H. S. P., et al. 2009, A&A, 499, 215
Belloche, A., Garrod, R. T., Müller, H. S. P., et al. 2025, A&A, 698, A143
Braakman, R., Drouin, B. J., Widicus Weaver, S. L., & Blake, G. A. 2010, J. Mol. Spectrosc., 264, 43
Brown, P. D., Charnley, S. B., & Millar, T. J. 1988, MNRAS, 231, 409
Carvajal, M., Favre, C., Kleiner, I., et al. 2019, A&A, 627, A65
Colzi, L., Martín-Pintado, J., Zeng, S., et al. 2024, A&A, 690, A121
Das, A., Majumdar, L., Sahu, D., et al. 2015, ApJ, 808, 21
Demaison, J., Boucher, D., BURIE, J., & Dubrulle, A. 1984, Z. Naturf. A, 39, 560
Demaison, J., Craig, N. C., Conrad, A. R., Tubergen, M. J., & Rudolph, H. D. 2012, J. Phys. Chem. A, 116, 9116
Endres, C. P., Schlemmer, S., Schilke, P., Stutzki, J., & Müller, H. S. P. 2016, J. Mol. Spectrosc., 327, 95
Fried, Z. T. P., Motiyenko, R. A., Sanz-Novo, M., et al. 2025, ApJ, 992, 187

Frisch, M. J., Trucks, G. W., Schlegel, H. B., et al. 2016, Gaussian~16 Revision C.01 (Wallingford, CT: Gaussian Inc.)
García de la Concepción, J., Jiménez-Serra, I., Corchado, J. C., et al. 2023, A&A, 675, A109
Garrod, R. T., & Pauly, T. 2011, ApJ, 735, 15
Grimme, S., Ehrlich, S., & Goerigk, L. 2011, J. Computat. Chem., 32, 1456
Herbst, E., Gianfranco, V., & Ceccarelli, C. 2020, ACS Earth Space Chem., 4, 488
Ilyushin, V. V., Margulès, L., Tercero, B., et al. 2021, J. Mol. Spectrosc., 379, 111454
Ioppolo, S., Kaňuchová, Z., James, R. L., et al. 2021, A&A, 646, A172
Ishibashi, A., Molpeceres, G., Hidaka, H., et al. 2024, ApJ, 976, 162
Jaman, A. I., Chakraborty, S., & Chakraborty, R. 2015, J. Mol. Struct., 1079, 402
Jiménez-Serra, I., Martín-Pintado, J., Rivilla, V. M., et al. 2020, Astrobiology, 20, 1048
Jiménez-Serra, I., Rodríguez-Almeida, L. F., Martín-Pintado, J., et al. 2022, A&A, 663, A181
Jiménez-Serra, I., Megías, A., Salaris, J., et al. 2025, A&A, 695, A247
Jones, P. A., Burton, M. G., Cunningham, M. R., et al. 2012, MNRAS, 419, 2961
Kolesniková, L., Peña, I., Alonso, E. R., et al. 2018, A&A, 619, A67
Li, J., Wang, J., Qiao, H., et al. 2020, MNRAS, 492, 556
Loomis, R. A., McGuire, B. A., Shingledecker, C., et al. 2015, ApJ, 799, 34
Marcelino, N., Tercero, B., Agúndez, M., & Cernicharo, J. 2021, A&A, 646, L9
Martín, S., Requena-Torres, M. A., Martín-Pintado, J., & Mauersberger, R. 2008, ApJ, 678, 245
Martín, S., Martín-Pintado, J., Blanco-Sánchez, C., et al. 2019, A&A, 631, A159
Medvedev, I. R., De Lucia, F. C., & Herbst, E. 2009, ApJS, 181, 433
Mininni, C., Beltrán, M. T., Rivilla, V. M., et al. 2020, A&A, 644, A84
Minissale, M., Congiu, E., Manicò, G., Pirronello, V., & Dulieu, F. 2013, A&A, 559, A49
Molpeceres, G., Enrique-Romero, J., Ishibashi, A., et al. 2025, MNRAS, 538, 1565
Neill, J. L., Muckle, M. T., Zaleski, D. P., et al. 2012, ApJ, 755, 153
Nguyen, H. V. L., Kleiner, I., Shipman, S. T., et al. 2014, J. Mol. Spectrosc., 299, 17
Oba, Y., Watanabe, N., Kouchi, A., Hama, T., & Pirronello, V. 2010, ApJ, 722, 1598
Peng, Y., Rivilla, V. M., Zhang, L., Ge, J. X., & Zhou, B. 2019, ApJ, 871, 251
Pickett, H. M. 1991, J. Mol. Spectrosc., 148, 371
Pickett, H. M., Poynter, R. L., Cohen, E. A., et al. 1998, J. Quant. Spec. Radiat. Transf., 60, 883
Remijan, A. J., Changala, P. B., Xue, C., et al. 2025, ApJ, 982, 191
Requena-Torres, M. A., Martín-Pintado, J., Rodríguez-Franco, A., et al. 2006, A&A, 455, 971
Requena-Torres, M. A., Martín-Pintado, J., Martín, S., & Morris, M. R. 2008, ApJ, 672, 352
Riveros, J. M. 1967, J. Chem. Phys., 46, 4605
Rivilla, V. M., Beltrán, M. T., Martín-Pintado, J., et al. 2017, A&A, 599, A26
Rivilla, V. M., Colzi, L., Jiménez-Serra, I., et al. 2022a, ApJ, 929, L11
Rivilla, V. M., Jiménez-Serra, I., Martín-Pintado, J., et al. 2022b, Front. Astron. Space Sci., 9, 829288
Rivilla, V. M., Sanz-Novo, M., Jiménez-Serra, I., et al. 2023, ApJ, 953, L20
Rodríguez-Almeida, L. F., Jiménez-Serra, I., Rivilla, V. M., et al. 2021a, ApJ, 912, L11
Rodríguez-Almeida, L. F., Rivilla, V. M., Jiménez-Serra, I., et al. 2021b, A&A, 654, L1
San Andrés, D., Rivilla, V. M., Colzi, L., et al. 2024, ApJ, 967, 39
Sanz-Novo, M., Belloche, A., Rivilla, V. M., et al. 2022, A&A, 666, A114
Sanz-Novo, M., Rivilla, V. M., Jiménez-Serra, I., et al. 2023, ApJ, 954, 3
Sanz-Novo, M., Rivilla, V. M., Jiménez-Serra, I., et al. 2024, ApJ, 965, 149
Sanz-Novo, M., Molpeceres, G., Rivilla, V. M., & Jimenez-Serra, I. 2025, A&A, 698, A36
Sanz-Novo, M., Rivilla, V. M., Endres, C. P., et al. 2025, ApJ, 980, L37
Savarese, A., Alessandrini, S., Melosso, M., et al 2025, ACS Earth Space Chem., 10, 198
Shingledecker, C. N., Álvarez-Barcia, S., Korn, V. H., & Kästner, J. 2019, ApJ, 878, 80
Shingledecker, C. N., Lamberts, T., Laas, J. C., et al. 2020, ApJ, 888, 52
Tercero, B., Cuadrado, S., López, A., et al. 2018, A&A, 620, L6
Tercero, B., Kleiner, I., Cernicharo, J., et al. 2013, ApJ, 770, L13
Tercero, F., López-Pérez, J. A., Gallego, J. D., et al. 2021, A&A, 645, A37
Wang, J., Marks, J. H., Turner, A. M., et al. 2023, Phys. Chem. Chem. Phys., 25, 936
Wang, J., Zhang, C., Marks, J. H., et al. 2024, Nat. Commun., 15, 10189
Zeng, S., Jiménez-Serra, I., Rivilla, V. M., et al. 2018, MNRAS, 478, 2962
Zeng, S., Zhang, Q., Jiménez-Serra, I., et al. 2020, MNRAS, 497, 4896
Zheng, S., Li, J., Wang, J., et al. 2024, ApJ, 961, 58
Zhou, Y., Quan, D.-H., Zhang, X., & Qin, S.-L. 2020, Res. Astron. Astrophys., 20, 125

Appendix A: Complementary tables and figures

In Tables A.1, A.2, A.3, A.4, A.5 and A.6 we provide the spectroscopic information of the transitions detected for methyl acetate, *a*-ethyl formate, *g*-ethyl formate, hydroxyacetone, lactaldehyde and methoxyacetaldehyde, respectively, which are shown in Figures 2, 3, A.1, 4, 5 and 6.

Regarding the preparation of the line catalog of methyl acetate in SPCAT format from the BELGI output, we also provide in Table A.1 the values of the line strength ($S_g\mu_g^2$; Tercero et al. 2013), which were used to compute the log I(nm^2 MHz) at 300 K via:

$$I(T) = 4.16231 \cdot 10^{-5} \cdot \nu \cdot g_I \cdot S_g \cdot \mu_g^2 \cdot \frac{\exp(-E''/kT) - \exp(-E'/kT)}{Q_r(T)}$$

with ν in MHz and μ in D.

We note that the original laboratory data covered up to J = 19 and $K_a \leq 7$, although predictions were initially computed up to J = 30 (Tercero et al. 2013). In this work, we adopt the rotational partition function values computed from first principles, derived from the rotational constants reported in Nguyen et al. (2014). Specifically, we obtained a Q_r (AA, 300 K) = 72174.2179 (without considering spin weights and all states), which is approximately 15% larger than the value used in Tercero et al. (2013) of Q_r (AA, 300 K) = 61648.6 (I. Kleiner, priv. communication). The latter was obtained by applying a correction factor of 2.6 to the Q_r (AA) computed through direct summation of the ground-state energy levels up to J = 30, which is needed to consider energy levels up to J = 65. Nevertheless, it may still underestimate the real partition function value if full convergence has not been achieved (Carvajal et al. 2019).

In contrast to the previous work, where each substate was treated as a separate species (Tercero et al. 2013), we have included all five substates in the same catalog. Consequently, the E_{up} (K) reported in Table A.1 accounts for the ZPE of the AA species (99.9450 cm^{-1}; Tercero et al. 2013). To consider all of the states and their weights, Q_r(Tot, 300 K) = Q_r (AA, 300 K) × f, where f = (16+16+16+8+8) = 64.

In Figure A.1 we show the tentative detection of *g*-ethyl formate, *g*-$CH_3CH_2OC(O)H$, toward G+0.693, while in Figures A.2 and A.3 we present the LTE simulation of the propionic acid and glycidol emission, respectively, using the upper limits to the column density derived toward G+0.693.

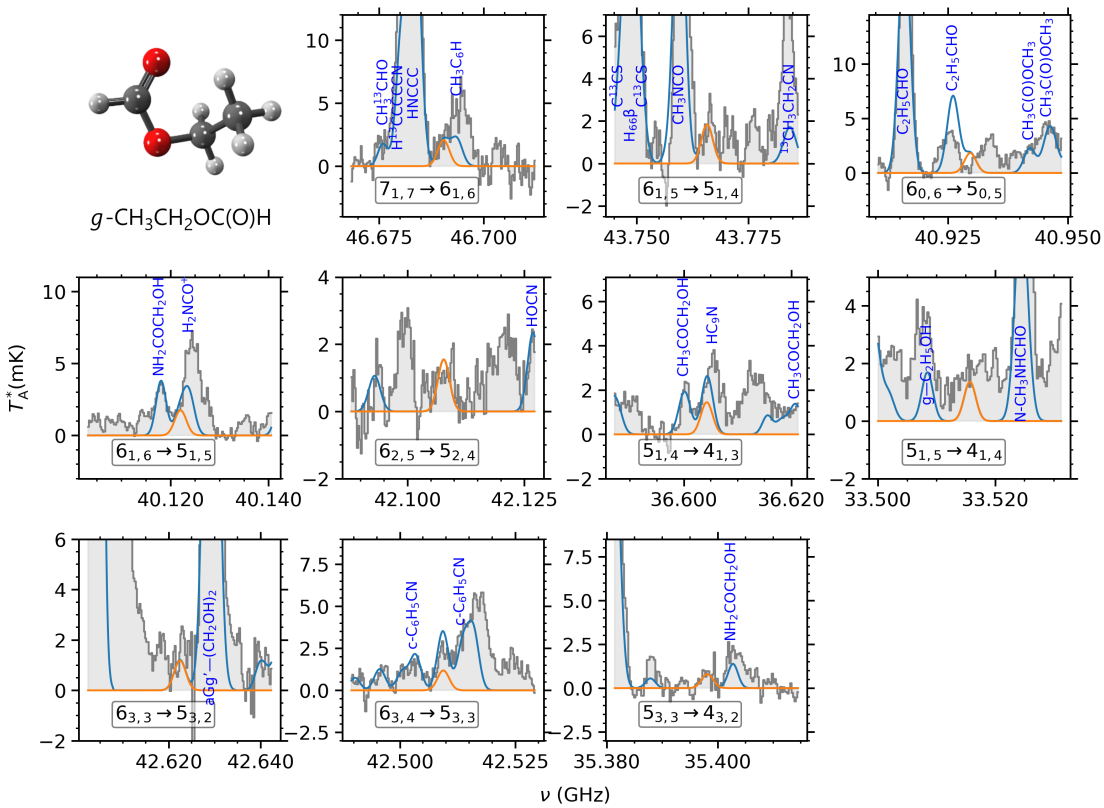

Fig. A.1: Tentative detection of *g*-ethyl formate, *g*-$CH_3CH_2OC(O)H$, toward G+0.693. The selected transitions are sorted by decreasing intensity and listed in Table A.3. The result of the LTE model of the *g*-$CH_3CH_2OC(O)H$ emission is shown in orange, together with the expected molecular emission from all the molecular species identified to date in our survey, including *g*-$CH_3CH_2OC(O)H$ (in blue), both overlaid on the observations (gray histogram). The molecular structure of *g*-$CH_3CH_2OC(O)H$ is also shown (C atoms in gray, O atoms in red and H atoms in white).

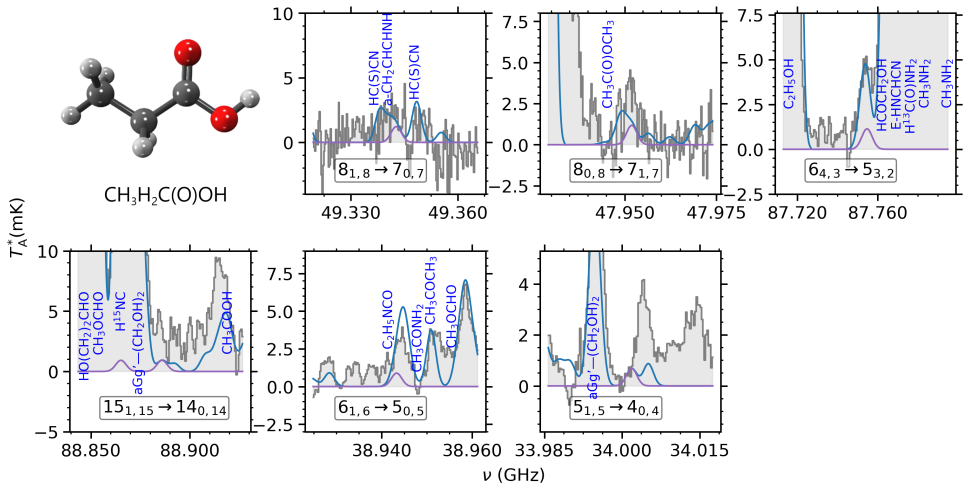

Fig. A.2: LTE simulation of the propionic acid, $CH_3CH_2C(O)OH$, emission using the upper limit column density derived toward G+0.693 (in purple) together with the expected molecular emission from all the molecular species identified to date in our survey (in blue), both overlaid on the observations (gray histogram). The quantum numbers for each transition are shown at the bottom of each panel.

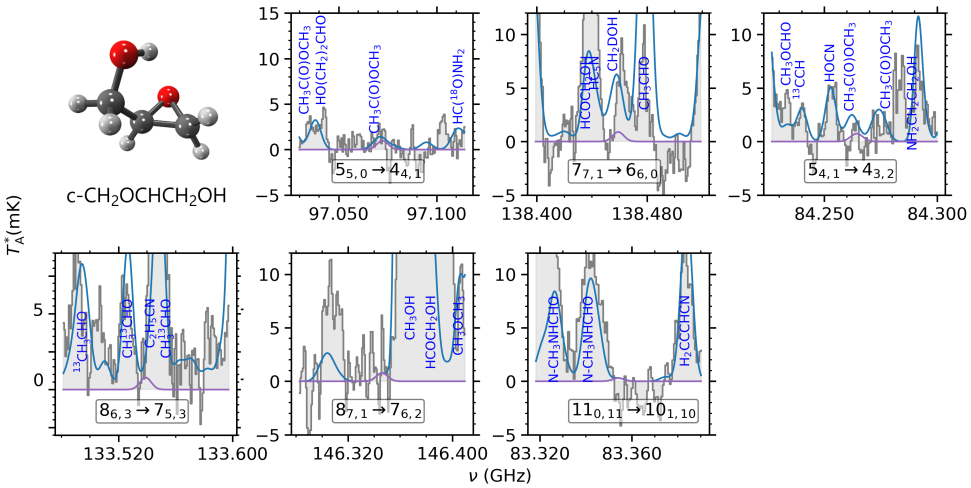

Fig. A.3: LTE simulation of the glycidol, (c-CH_2OCHCH_2OH, emission using the upper limit column density derived toward G+0.693 (in purple) together with the expected molecular emission from all the molecular species identified to date in our survey (in blue), both overlaid on the observations (gray histogram). The quantum numbers for each transition are shown at the bottom of each panel.

Table A.1: Spectroscopic information of the selected transitions of methyl acetate detected toward G+0.693, shown in Figure 2.

Frequency (GHz)	Transition[a]	$S_g\mu_g^2$	log I at 300 K (nm^2 MHz)	E_{up} (K)	Blending
32.797604 (2)	$6_{3,3}$–$6_{2,4}$ (E_3)	8.19	–7.0096	12.2	Unblended
32.840814 (2)	$6_{3,3}$–$6_{2,4}$ (E_1)	8.20	–7.0081	12.2	Slightly blended: U-line
34.628602 (2)	$4_{3,1}$–$4_{2,2}$ (E_3)	4.70	–7.1979	8.3	Unblended
34.637085 (4)	$8_{3,6}$–$8_{2,7}$ (E_4)	9.69	–6.8957	16.9	Slightly blended: U-line
34.715239 (4)	$8_{3,6}$–$8_{2,7}$ (E_3)	9.67	–6.8947	16.9	Unblended
35.446462 (2)	$5_{1,5}$–$4_{0,4}$ (E_4)	9.56	–6.8672	6.7	Slightly blended: U-line
35.452045 (2)	$5_{1,5}$–$4_{0,4}$ (E_1)	9.56	–6.8669	6.7	Unblended
35.454312 (2)	$5_{1,5}$–$4_{0,4}$ (E_3)	9.56	–6.8667	6.7	Unblended
38.523669 (4)	$9_{3,7}$–$9_{2,8}$ (E_1)	10.81	–6.7608	20.1	Blended: U line
38.537458 (2)	$6_{0,6}$–$5_{1,5}$ (E_3)	11.85	–6.7036	8.6	Unblended
38.539998 (2)	$6_{0,6}$–$5_{1,5}$ (E_1)	11.85	–6.7036	8.6	Unblended
38.543524 (2)	$6_{0,6}$–$5_{1,5}$ (E_4)	11.85	–6.7036	8.6	Slightly blended: U-line
38.549823 (4)	$9_{3,7}$–$9_{2,8}$ (E_3)	10.80	–6.7603	20.1	Blended: U-line
40.941899 (2)	$6_{1,6}$–$5_{0,5}$ (E_4)	12.20	–6.6386	8.6	Slightly blended: U-line
40.945609 (2)	$6_{1,6}$–$5_{0,5}$ (E_1)	12.20	–6.6385	8.6	Unblended
40.946537 (2)	$6_{1,6}$–$5_{0,5}$ (E_3)	12.20	–6.6384	8.6	Unblended
41.235605 (2)	$6_{1,6}$–$5_{0,5}$ (E_2)	12.29	–6.6266	7.0	Unblended
41.237259 (2)	$6_{1,6}$–$5_{0,5}$ (AA)	12.29	–6.6265	7.0	Unblended
42.640369 (4)	$6_{4,3}$–$6_{3,4}$ (E_4)	7.13	–6.8433	13.6	Slightly blended: U-line
46.805363 (2)	$7_{1,7}$–$6_{0,6}$ (E_2)	14.97	–6.4339	9.2	Unblended
46.805610 (10)	$12_{2,10}$–$12_{1,11}$ (E_3)	13.55	–6.5093	31.4	Unblended
46.806655 (2)	$7_{1,7}$–$6_{0,6}$ (AA)	14.97	–6.4338	9.2	Unblended
46.811991 (10)	$12_{2,10}$–$12_{1,11}$ (E_4)	13.55	–6.5093	31.4	Slightly blended: U-line
46.812678 (10)	$12_{2,10}$–$12_{1,11}$ (E_1)	13.55	–6.5091	31.4	Slightly blended: U-line
76.613177 (9)	$12_{0,12}$–$12_{1,11}$ (E_3)	28.59	–5.7486	26.3	Slightly blended: $NH_2CH_2CH_2OH$
76.613332 (9)	$12_{0,12}$–$12_{1,11}$ (E_4)	28.59	–5.7486	26.3	Slightly blended: $NH_2CH_2CH_2OH$
76.613594 (9)	$12_{0,12}$–$12_{1,11}$ (E_1)	28.59	–5.7485	26.2	Slightly blended: $NH_2CH_2CH_2OH$
83.789892 (4)	$5_{4,1}$–$4_{3,2}$ (AA)	9.26	–6.1373	10.4	Slightly blended: C_2H_5OCHO
88.939251 (15)	$14_{0,14}$–$13_{1,13}$ (E_3)	34.01	–5.5552	34.5	Blended: t-C_2H_3CHO
88.939307 (15)	$14_{0,14}$–$13_{1,13}$ (E_4)	34.01	–5.5552	34.5	Blended: t-C_2H_3CHO
88.939623 (15)	$14_{0,14}$–$13_{1,13}$ (E_1)	34.01	–5.5551	34.5	Blended: t-C_2H_3CHO
88.953729 (15)	$14_{1,14}$–$13_{0,13}$ (E_3)	34.01	–5.5550	34.5	Unblended
88.953732 (15)	$14_{1,14}$–$13_{0,13}$ (E_4)	34.01	–5.5550	34.5	Unblended
88.954100 (15)	$14_{1,14}$–$13_{0,13}$ (E_1)	34.01	–5.5550	34.5	Unblended
94.160620 (5)	$7_{4,4}$–$6_{3,4}$ (E_1)	9.13	–6.0496	16.0	Unblended
94.166317 (5)	$7_{4,4}$–$6_{3,4}$ (E_3)	9.13	–6.0495	16.1	Unblended
94.313817 (14)	$14_{1,13}$–$13_{2,12}$ (E_3)	26.70	–5.6141	37.9	Slightly blended: $CH_3{}^{13}CH_2OH$
94.314988 (14)	$14_{1,13}$–$13_{2,12}$ (E_4)	26.70	–5.6141	37.9	Slightly blended: $CH_3{}^{13}CH_2OH$
94.315443 (14)	$14_{1,13}$–$13_{2,12}$ (E_1)	26.70	–5.6141	37.9	Slightly blended: $CH_3{}^{13}CH_2OH$
95.078847 (16)	$14_{2,13}$–$13_{1,12}$ (E_2)	26.65	–5.6057	36.4	Slightly blended: $HCOCH_2OH$
95.080895 (16)	$14_{2,13}$–$13_{1,12}$ (AA)	26.65	–5.6057	36.4	Unblended
95.095381 (18)	$15_{0,15}$–$14_{1,14}$ (E_3)	36.71	–5.4702	39.1	Unblended
95.095417 (18)	$15_{0,15}$–$14_{1,14}$ (E_4)	36.71	–5.4702	39.1	Unblended
95.095735 (18)	$15_{0,15}$–$14_{1,14}$ (E_1)	36.71	–5.4702	39.1	Unblended
95.102484 (18)	$15_{1,15}$–$14_{0,14}$ (E_3)	36.71	–5.4701	39.1	Unblended
95.102496 (18)	$15_{1,15}$–$14_{0,14}$ (E_4)	36.71	–5.4702	39.1	Unblended
95.102840 (18)	$15_{1,15}$–$14_{0,14}$ (E_1)	36.71	–5.4701	39.1	Unblended
98.823558 (5)	$7_{4,3}$–$6_{3,3}$ (E_1)	9.40	–5.9965	17.0	Slightly blended: CH_3COCH_3
98.826693 (4)	$7_{4,3}$–$6_{3,3}$ (E_4)	9.40	–5.9965	17.0	Slightly blended: CH_3COCH_3
101.249746 (22)	$16_{0,16}$–$15_{1,15}$ (E_3)	39.41	–5.3917	43.9	Slightly blended: C_2H_5SH
101.249772 (22)	$16_{0,16}$–$15_{1,15}$ (E_4)	39.41	–5.3917	43.9	Slightly blended: C_2H_5SH
101.250085 (22)	$16_{0,16}$–$15_{1,15}$ (E_1)	39.41	–5.3917	43.9	Slightly blended: C_2H_5SH
101.253205 (22)	$16_{1,16}$–$15_{0,15}$ (E_3)	39.41	–5.3917	43.9	Slightly blended: C_2H_5SH
101.253219 (22)	$16_{1,16}$–$15_{0,15}$ (E_4)	39.41	–5.3917	43.9	Slightly blended: C_2H_5SH
101.253545 (22)	$16_{1,16}$–$15_{0,15}$ (E_1)	39.41	–5.3917	43.9	Slightly blended: C_2H_5SH

Notes. [a] The AA, E_1, E_2 and E_3 and E_4 labels refer to the different symmetry or torsional substates, arising from the presence of two non-equivalent CH_3 internal rotation motions. Numbers in parentheses represent the predicted uncertainty associated to the last digits. We denote as U-line the line blending with a yet unidentified feature, and as "unblended" lines those that are not contaminated by other species, although many transitions belonging to different symmetry substates are partially or fully coalesced (auto-blended).

Table A.2: Spectroscopic information of the transitions of *a*-ethyl formate detected toward G+0.693−0.027, shown in Figure 3.

Frequency (GHz)	Transition[(a)]	log I (300 K) (nm^2 MHz)	E_{up} (K)	Blending
31.8852150 (19)	$6_{1,6}$–$5_{1,5}$	-6.1602	6.0	Blended: C_6H
32.7188633 (19)	$6_{0,6}$–$5_{0,5}$	-6.1251	5.5	Blended: $H_{83}\gamma$
32.8790743 (19)	$6_{2,5}$–$5_{2,4}$	-6.1757	8.3	Unblended
33.8355565 (19)	$6_{1,5}$–$5_{1,4}$	-6.1090	6.4	Slightly blended: CH_3CHCO
38.3453139 (22)	$7_{2,6}$–$6_{2,5}$	-5.9635	10.2	Slightly blended: $HCCCH_2CN$
38.4274410 (22)	$7_{3,5}$–$6_{3,4}$	-6.0180	13.8	Blended: $HCCCH_2CN$
38.4342157 (22)	$7_{3,4}$–$6_{3,3}$	-6.0178	13.8	Slightly blended: U-line
38.6374107 (22)	$7_{2,5}$–$6_{2,4}$	-5.9570	10.2	Blended: $H_{86}\delta$
39.4528074 (22)	$7_{1,6}$–$6_{1,5}$	-5.9080	8.2	Slightly blended: U-line
42.4683643 (25)	$8_{1,8}$–$7_{1,7}$	-5.7861	9.8	Blended: $^{13}CH_3CH_2CN$
43.8052932 (25)	$8_{2,7}$–$7_{2,6}$	-5.7838	12.3	Slightly blended: $HCCCH_2CN$
44.2387698 (25)	$8_{2,6}$–$7_{2,5}$	-5.7753	12.3	Slightly blended: U-line *
45.0591299 (25)	$8_{1,7}$–$7_{1,6}$	-5.7354	10.4	Unblended
48.7428006 (27)	$9_{0,9}$–$8_{0,8}$	-5.6117	11.7	Unblended
49.2581397 (27)	$9_{2,8}$–$8_{2,7}$	-5.6280	14.6	Slightly blended: $HCCCH_2CN$
49.8680897 (27)	$9_{2,7}$–$8_{2,6}$	-5.6174	14.7	Unblended

Notes. [(a)] The rotational energy levels are labeled using the conventional notation for asymmetric tops: J_{K_a,K_c}. Numbers in parentheses represent the predicted uncertainty associated to the last digits. Transitions that were not used in the AUTOFIT owing to a non-negligible contamination with a U-line are flagged with an asterisk (*).

Table A.3: Spectroscopic information of the transitions of *g*-ethyl formate detected toward G+0.693−0.027, shown in Figure A.1.

Frequency (GHz)	Transition[(a)]	log I (300 K) (nm^2 MHz)	E_{up} (K)	Blending
33.515573 (29)	$5_{1,5}$–$4_{1,4}$	-6.0284	5.1	Blended: U-line *
35.398028 (20)	$5_{3,3}$–$4_{3,2}$	-6.1600	7.8	Unblended
36.604135 (25)	$5_{1,4}$–$4_{1,3}$	-5.9528	5.6	Blended HC_9N and U-line *
40.121894 (74)	$6_{1,6}$–$5_{1,5}$	-5.7904	7.0	Blended: H_2NCO and U-line *
40.929526 (64)	$6_{0,6}$–$5_{0,5}$	-5.7656	6.9	Blended: C_2H_5CHO
42.107618 (48)	$6_{2,5}$–$5_{2,4}$	-5.7887	8.3	Unblended
42.509261 (48)	$6_{3,4}$–$5_{3,3}$	-5.8557	9.9	Blended
42.622312 (49)	$6_{3,3}$–$5_{3,2}$	-5.8534	9.9	Blended: U-line *
43.765633 (58)	$6_{1,5}$–$5_{1,4}$	-5.7165	7.6	Unblended
46.69026 (16)	$7_{1,7}$–$6_{1,6}$	-5.5918	9.2	Blended: CH_3C_6H and U-line *

Notes. [(a)] The rotational energy levels are labeled using the conventional notation for asymmetric tops: J_{K_a,K_c}. Numbers in parentheses represent the predicted uncertainty associated to the last digits. Transitions that were not used in the AUTOFIT owing to a non-negligible contamination with a U-line are flagged with an asterisk (*).

Table A.4: Spectroscopic information of the transitions of hydroxyacetone detected toward G+0.693−0.027, shown in Figure 4.

Frequency (GHz)	Transition[(a)]	log I (300 K) (nm^2 MHz)	E_{up} (K)	Blending
34.06171 (10)	$5_{1,5}$–$4_{0,4}$ (A)	-5.9719	4.7	Unblended
35.10788 (10)	$6_{0,6}$–$5_{1,5}$ (A)	-5.8670	6.4	Slightly blended: $H^{13}CC^{13}CN$
36.6000352 (10)	$6_{3,4}$–$6_{2,5}$ (A)	-5.9821	9.7	Blended: $CH_3C(O)OCH_3$
36.62067 (10)	$6_{1,6}$–$5_{1,5}$ (A)	-5.9796	9.7	Blended: U-line *
37.44757 (10)	$6_{0,6}$–$5_{0,5}$ (A)	-5.9551	6.4	Unblended
38.96035 (10)	$6_{1,6}$–$5_{0,5}$ (A)	-5.7582	9.7	Blended: cis-CH_3OCHO
41.0700049 (58)	$6_{2,4}$–$5_{2,3}$ (E)	-5.9122	11.3	Slightly blended: U-line
41.0755430 (35)	$6_{2,5}$–$5_{2,4}$ (E)	-5.9617	10.5	Slightly blended: U-line
42.5091837 (15)	$7_{1,7}$–$6_{1,6}$ (A)	-5.7830	8.5	Slightly blended: g-C_2H_5OCHO
42.5817854 (29)	$7_{1,7}$–$6_{1,6}$ (E)	-5.8027	11.3	Blended: U-line *
43.0928962 (15)	$7_{0,7}$–$6_{0,6}$ (A)	-5.7689	8.5	Unblended
44.0219474 (21)	$7_{1,7}$–$6_{0,6}$ (A)	-5.5687	8.5	Blended: Aa-n-C_3H_7OH
44.808245 (47)	$9_{4,5}$–$9_{3,6}$ (A)	-5.6091	19.8	Unblended
46.0448088 (31)	$7_{2,6}$–$6_{2,5}$ (A)	-5.7438	10.2	Unblended
47.7984158 (16)	$8_{0,8}$–$7_{1,7}$ (A)	-5.4297	10.8	Unblended

Notes. [(a)] The rotational energy levels are labeled using the conventional notation for asymmetric tops: J_{K_a,K_c}. Numbers in parentheses represent the predicted uncertainty associated to the last digits. The A and E labels refer to the A- and E- symmetry states of hydroxyacetone, arising due to the presence of a methyl internal rotation motion. Transitions that were not used in the AUTOFIT owing to a non-negligible contamination with a U-line are flagged with an asterisk (*).

Table A.5: Spectroscopic information of the transitions of lactaldehyde detected toward G+0.693−0.027, shown in Figure 5.

Frequency (GHz)	Transition[(a)]	log I (300 K) (nm^2 MHz)	E_{up} (K)	Blending
32.8030391 (7)	$5_{0,5}$–$4_{1,4}$	-5.8204	5.0	Unblended
34.8797382 (13)	$9_{4,6}$–$9_{3,7}$	-5.6662	19.7	Blended: aGg'-$(CH_2OH)_2$ *
34.9104833 (7)	$5_{1,5}$–$4_{0,4}$	-5.7505	5.1	Blended: U-line *
39.6056410 (8)	$6_{0,6}$–$5_{1,5}$	-5.5481	7.0	Unblended
39.8461672 (16)	$9_{5,4}$–$9_{4,5}$	-5.5811	21.7	Slightly blended: U-line *
40.7250108 (8)	$6_{1,6}$–$5_{0,5}$	-5.5188	7.0	Unblended
46.1743922 (9)	$7_{0,7}$–$6_{1,6}$	-5.3312	9.2	Blended: $^{13}CH_2CHCN$
85.7293506 (14)	$7_{4,3}$–$6_{3,4}$	-5.0545	13.6	Unblended *
101.649525 (50)	$8_{5,4}$–$5_{4,3}$	-4.7871	18.4	Blended: C_2H_3CN *
103.911545 (50)	$7_{6,2}$–$6_{5,1}$	-4.6700	18.0	Blended: N-CH_3NHCHO
103.9116165 (19)	$7_{6,1}$–$6_{5,1}$	-5.3245	18.0	Blended: N-CH_3NHCHO
103.9130904 (19)	$7_{6,2}$–$6_{5,2}$	-5.3245	18.0	Blended: N-CH_3NHCHO
103.913219 (50)	$7_{6,1}$–$6_{5,2}$	-4.6700	18.0	Blended: N-CH_3NHCHO
137.629993 (50)	$9_{8,2}$–$8_{7,1}$	-4.3056	30.3	Blended: $CH_3C(O)OCH_3$
137.629993 (50)	$9_{8,1}$–$8_{7,1}$	-4.9688	30.3	Blended: $CH_3C(O)OCH_3$
137.629993 (50)	$9_{8,2}$–$8_{7,2}$	-4.9688	30.3	Blended: $CH_3C(O)OCH_3$
137.629993 (50)	$9_{8,1}$–$8_{7,2}$	-4.3056	30.3	Blended: $CH_3C(O)OCH_3$

Notes. [(a)] The rotational energy levels are labeled using the conventional notation for asymmetric tops: J_{K_a,K_c}. Numbers in parentheses represent the predicted uncertainty associated to the last digits. Transitions that were not used in the AUTOFIT owing to a non-negligible contamination with a U-line or a lower S/N ratio are flagged with an asterisk (*).

Table A.6: Spectroscopic information of the transitions of methoxyacetaldehyde detected toward G+0.693−0.027, shown in Figure 6.

Frequency (GHz)	Transition[(a)]	log I (300 K) (nm^2 MHz)	E_{up} (K)	Blending
35.42961 (15)	$8_{1,8}$–$7_{1,7}$	-5.1429	8.8	Unblended
35.84289 (15)	$8_{0,8}$–$7_{0,7}$	-5.1243	7.7	Slightly blended: $^{13}CH_2CHCN$
39.85602 (15)	$9_{1,9}$–$8_{1,8}$	-4.9907	10.7	Unblended
40.3145715 (17)	$9_{0,9}$–$8_{0,8}$	-4.9737	9.6	Unblended
40.3896344 (17)	$9_{2,7}$–$8_{2,6}$	-5.0014	14.6	Slightly blended: U-line
44.2818158 (23)	$10_{1,10}$–$9_{1,9}$	-4.8554	12.9	Slightly blended: U-line
44.7831474 (18)	$10_{0,0}$–$9_{0,9}$	-4.8396	11.7	Blended: CH_3C_4H
44.8303900 (18)	$10_{2,9}$–$9_{2,8}$	-4.8637	16.8	Blended: $H^{13}COOH$
44.8860560 (19)	$10_{2,8}$–$9_{2,7}$	-4.8626	16.8	Blended: U-line *
45.3688132 (25)	$10_{1,9}$–$9_{1,8}$	-4.8347	13.1	Blended: C_2H_5CHO
49.2483433 (20)	$11_{0,11}$–$10_{0,10}$	-4.7190	14.1	Blended: $CH_3{}^{34}SH$

Notes. [(a)] The rotational energy levels are labeled using the conventional notation for asymmetric tops: J_{K_a,K_c}. Numbers in parentheses represent the predicted uncertainty associated to the last digits. Transitions that were not used in the AUTOFIT owing to a non-negligible contamination with a U-line are flagged with an asterisk (*).